On the aerodynamic performance of redundant propellers for multi-rotor eVTOL in cruise

Tao Zhang [a], G.N. Barakos [b,*], Furqan [c]

[a] *School of Engineering, University of Leicester, LE1 7RH Leicester, UK*
[b] *CFD Laboratory, School of Engineering, University of Glasgow, G12 8QQ Glasgow, UK*
[c] *GKN Aerospace, BS34 9AU Bristol, UK*

ARTICLE INFO

ABSTRACT

As multi-rotor and convertible configurations gain compelling popularity in Advanced Air Mobility designs, the handling of redundant propellers during cruise flight regimes becomes a new challenge. This paper presents a systematic study of the aerodynamic performance of feathered and windmilling redundant propellers on a simplified multi-rotor, multi-wing configuration. High-fidelity CFD simulations were performed with a systematic test matrix including the blade feathering angle, azimuth shift, coning angle, and windmilling pitch angle and RPM. For the feathered blades, the feathering angle had a strong impact on the aerodynamic performance. The feathered blades could substantially reduce the overall lift and increase the overall drag at high feathering angles (up to 25% lift reduction and 70% drag increase). This is correlated with changes in the sectional wing inflow angles induced by the upstream feathered blades. Windmilling propellers, in ideal cases, were found capable of considerable wind energy extraction (50% of required cruise power) and could create slowed inflows for downstream thrusting propellers, at the cost of excessive drag (up to 90% more). Comparisons of vehicle performance with feathered and windmilling blades, showed similar aerodynamic forces and energy consumption. This shows that windmilling could be a feasible option for redundant propellers, given careful balancing of the drag and energy conversions. The presented results provide valuable guidance for the handling of redundant blades, for future multi-rotor aircraft designs for sustainable aviation.

1. Introduction

In recent years, multi-rotor and convertible aircraft configurations have gained popularity in emerging Advanced Air Mobility designs [1]. These unconventional configurations are promising candidates for electric Vertical Take-off and Landing (eVTOL) vehicles, aiming at decarbonising aviation while transforming future transport. In hover or vertical take-off/landing, the rotary wings provide the necessary lift against the vehicle weight. In such cases, multiple rotary wing systems are critical for efficiency, acoustics, and particularly safety considerations.

In cruise flight, however, the lift is usually supplied by lifting surfaces, and the thrust needed (to counter the drag) is only a small fraction of what is necessary in vertical flight. In this case, it is preferred to shut down some of the propellers and have others thrusting at optimal efficiency. This leads to the problem of redundant inoperative propellers for multi-rotor eVTOLs in cruise. These redundant propellers can produce significant drag, due to the large number of rotors and blades, and

the big rotor size designed for hover. Moreover, because of the complex multi-rotor configuration, these redundant propellers may lead to substantial aerodynamic interference with downstream lifting surfaces and rotary wings. While the aerodynamic interactions between thrusting propellers and wings have been quite extensively studied [2–4], few have investigated the interference due to redundant blades.

Current options for these redundant or inoperative propellers are generally folding or retracting, feathering, and windmilling. Some eVTOL designs adopt separate thrusting and lifting rotary wings systems, and the lifting propellers are left inoperative in cruise. These redundant propellers also create significant drag, and folding or retracting are recommended by recent experimental studies [5,6]. This obviously minimises the aerodynamic impacts, as the redundant blades are removed from the aerodynamic considerations. However, this increases the mechanical and structural complexity. Extra space and weight are needed to house the blades when retracted, especially for large blades designed for hover.

Nomenclature

Latin

AoA	Angle of Attack, °
b	Wing Span Length, m
Cp	Pressure Coefficient, $Cp = \frac{p-p_\infty}{0.5\rho V_\infty^2}$
D	Drag, N
L	Lift, N
p	Pressure, Pa
P	Required cruise power, $P = DV_\infty$, W
P_c, P_e	Propeller power consumption and extraction, W
RPM	Rotation Per Minute, [-]
u, v, w	Flow velocity along 3D Cartesian directions, m/s
V	Flow velocity magnitude, m/s
$\mathbf{W}$	Conservative Flow Variables

Greek

α	Angle of attack, °
β	Blade conning angle, °

$\psi, \delta\psi$	Blade azimuth angle and azimuth shift, °
ρ	Density, kg/m^3
θ	Feathering angle or windmilling pitch angle at 75% blade span, °

Subscripts and superscripts

0	Clean airframe values
i, j, k	Grid block indices in 3D
f, m, a	Front, middle, aft wing values
x, y, z	3D Cartesian directions
∞	Free-stream Value

Acronyms

CFD	Computational Fluid Dynamics
eVTOL	electric Vertical Take-off and Landing
HMB3	Helicopter Multi-Block 3 solver
URANS	Unsteady Reynolds Averaged Navier Stokes

Feathering is the typical option for inoperative propellers in cruise, for conventional fixed-wing aircraft. Feathering refers to stopping the propeller rotation and pitching the blades to be parallel to the air flow. This idea can be dated back to the 1930s [7,8] as soon as variable blade pitch propellers became available, and has since become a default requirement for propeller designs [9]. Early studies [7,8] found that feathering the blades would help stop the engine rotation in case of an engine failure, and derive limited drag and impact on the overall aircraft performance. While this holds for conventional fixed-wing aircraft with small thrusting propellers, for novel eVTOL designs with larger propellers designed for both thrusting and lifting purposes, the drag can be significant, and the downstream aerodynamic interference can be substantial [10]. At present, no study has investigated this new problem to guide the feathering option for multi-rotor eVTOL designs.

Another option is to windmill the redundant propellers. In this case, the propeller rotates driven by the air flow, and this produces drag. Another pitfall is that the windmilling keeps the engine rotating, and this could lead to further mechanical and heating problems. Indeed, windmilling is not a popular option for conventional fixed-wings with inoperative propellers. However, with novel electric propulsion, the windmilling option could be attractive. This is because electric motors allow windmilling propellers to directly convert wind energy to electricity, like an airborne power generation system [11]. The extra windmilling drag could also be exploited to control the vehicle speed while recycling the kinetic energy. Sinnige et al. [4] studied the performance a wing-tip-mounted propeller in windmilling. While harvesting the wind energy, they found that the windmilling propeller wake had an important impact on the wing performance, depending on the swirl direction of the blades. For multi-rotor eVTOL designs in cruise, and given careful arrangements, this may derive further benefits as a swirl recovery condition, along with the slowed inflow velocities due to energy extraction, for downstream thrusting propellers. These are also rarely investigated and need to be understood for improved design and operation.

The lack of quantitative understanding of the importance of redundant propellers, and of the associated aerodynamic interference in cruise, hinders the development of multi-rotor eVTOLs for future aviation. To narrow this knowledge gap, this paper presents a systematic investigation of the feathering and windmilling options for redundant propellers for multi-rotor eVTOLs in cruise. The objectives are to understand the aerodynamic performance, and particularly the downstream aerodynamic interference brought by different redundant propeller handlings. The high-fidelity results and analyses provide valuable guidance for aircraft design and operation for future electric aviation.

The contents of this work are organised as follows. Section 2 presents a simplified multi-rotor, multi-wing eVTOL model [10,12]. The redundant propeller was mounted at the upstream front wingtip to induce downstream interference. Section 3 presents details of the modelling methodologies and tools. Section 4 analyses the feathering performance variations, while Section 5 discusses the detailed aerodynamic interference. Section 6 presents the windmilling performance over a wide range of blade pitch angles and rotational speeds, including comparisons between complete vehicle performance with feathered and windmilling propellers. Section 7 summarises the work and draws conclusions.

2. Model and case descriptions

2.1. A simplified multi-rotor eVTOL model

The current study focuses on a simplified, half-model of the GKN Skybus design [10,12] in cruise flight. The model is shown in Fig. 1. The complete Skybus design consists of an airframe with six tandem wings and six propellers. The propellers are mounted at the tips of the wings and are tiltable to change the thrust line to convert between hover and cruise modes. The propellers have six blades and a radius of $R = 3.25$ m. These large propellers were designed to carry the heavy vehicle weight in hover, and become redundant in cruise due to the lower thrust requirement. The large propeller size is typical for tilt-rotor designs, and the detailed geometric definition can be found in Ref [12]. The geometric sizes of the airframe are presented in Fig. 1 relative to the rotor radius. For this multi-wing design, the front-wing has a 5-degree anhedral angle, while the aft wing has a 10-degree dihedral angle to reduce interference as detailed in Ref [10].

To begin this study, a propeller is considered mounted at tip of the front wing. This choice is to place the blades at the upstream-most position, so that it generates maximised aerodynamic interference for downstream components for the study. The free-stream speed is set to 90 m/s with zero incidence or sideslip. A lateral symmetric plane is assumed at the centre of the fuselage as shown in Fig. 1. The propeller was tiltable and was designed to produce thrust in cruise or lift in hover. In thrusting conditions, the propellers are designed to rotate top-in. This may deteriorate the aerodynamic performance, but brings strong acoustic benefits [13].

However, in this work, this propeller was assumed redundant to evaluate two options, i.e. feathering and windmilling. While windmilling, the blades rotate in top-out direction driven by the in-plane forces, which is opposite to the thrusting condition. This creates a
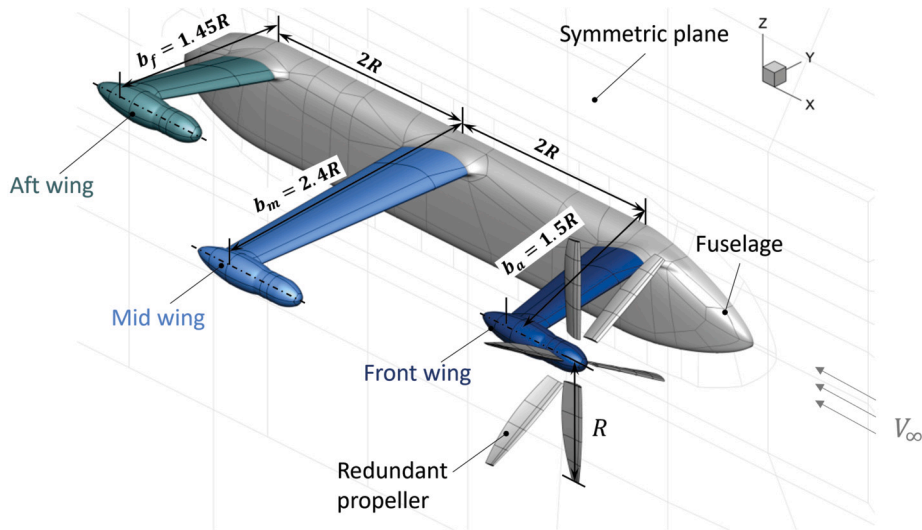
Fig. 1. Simplified Skybus [10] half-model for the study of redundant propeller handling in cruise.

Table 1
Test matrix for the study of redundant propeller aerodynamic interactions.

Case series	Propeller status	75% feathering angle θ/[deg]	Azimuth shift $\delta\psi$/[deg] θ/[deg]	Coning angle β/[deg]	Windmill RPM/[-]
1	feathered	80, 85, 90, 95, 100	0	0	-
2	feathered	85, 90, 95	30	0	-
3	feathered	85	0	-5, 0, 5, 10, 15	-
4	Windmilling	85, 90, 95, 100	-	0	0, 30, 60, 90, 120

weak swirl recovery condition benefiting any downstream thrusting propellers. In the windmilling case, the blades are highly pitched with the nominal pitch angle at 75% blade span generally greater than 90 degrees.

This isolated front propeller case is a baseline and is used as a starting point for this aerodynamic interaction study. This supports the quantification of its effects on downstream components, and the complete interference study (with all propellers installed) can be evaluated later, following a build-up approach. Downstream propellers are hence removed to reduce the problem variables and complexity in this study.

2.2. Test matrix

The current study focuses on two options for redundant propellers in cruise flight, i.e. feathering and windmilling. The complete investigation matrix for this study is presented in Table 1. Cases 1, 2, and 3 evaluate the effect of feathering blades, while Case 4 investigates the windmilling option. A further Case 5 (Table 3) evaluated the entire vehicle performance with all propellers installed in later sections, but with different feathering and windmilling options.

Cases 1, 2, 3 focus on the effects of feathering angle θ, azimuth shift $\delta\psi$, and blade coning angles β. Case 1 evaluates the effects of blade feathering angles as defined in Fig. 2(a), with the blade feathering angle (measured at 75%) varied from 80 degrees to 100 degrees (all blades had the same feathering angle). Note the windmilling pitch angle had the same definition as the feathering angle. The blades had zero azimuth shift and zero cone angle. Note that at the initial feathering of 80 degrees, the inboard blades (pointing towards the fuselage) generally produce lift, while the outboard blades produce downwards forces. However, as the feathering angle is increased and due to the blade's non-linear twist, the blade sectional lift contributions vary and may change signs. The feathering angle is expected to have direct impact on the feathered blade drag and its downstream aerodynamic inter-

ference needs to be evaluated. Case 1 is the baseline case for further analysis.

Case 2 is derived from Case 1 by introducing a 30-degree azimuth shift, as defined in Fig. 2(b). The azimuth shift $\delta\psi$ was introduced to change the blades' azimuth positions by rotating about the shaft. This is to understand if feathering the blades at certain azimuth position would result in particular benefits, and how would this impact the downstream interference. The feathering angle in this case was also varied to evaluate the responses.

Case 3 is also derived from Case 1, and the blades were added forward and backward cone angles, as defined in Fig. 2(c). This is similar to partially folding the blades. A fully-folded or retracted propeller was expected to induce the minimum interference, but this may not be feasible due to the blade size and the restricting mechanical complexity. Partially folding the blades, i.e. adding cone angles is a more practical option, and is also ideal for immediate deployment in the case of emergency.

The windmilling option was investigated with Case 4 of Table 1. In this case, the blades were allowed to rotate, driven by the in-plane forces due to the free-stream. The windmilling rotational direction was opposite to the thrusting direction as shown in Fig. 2(b). For eVTOL vehicles, since the propellers are driven by electric motors, they can directly convert wind energy to electricity. Although the drag is expected to increase due to windmilling, this may still be beneficial since it generates power and creates a slowed inflow for downstream propellers. In the present investigation of windmilling, a range of blade pitch/RPM combinations were studied to inspect the power generation performance.

Numerical simulations used the same grid components, but the blade grids were rotated and transformed, as necessary, to change the corresponding θ, $\delta\psi$, and β. Simulations of Cases 1, 2, and 3 were conducted as steady-state without moving parts, while the windmilling simulations for Case 4 used a temporal resolution of 1-degree-per-step for the windmilling blades. The analyses focused on the overall lift and drag,
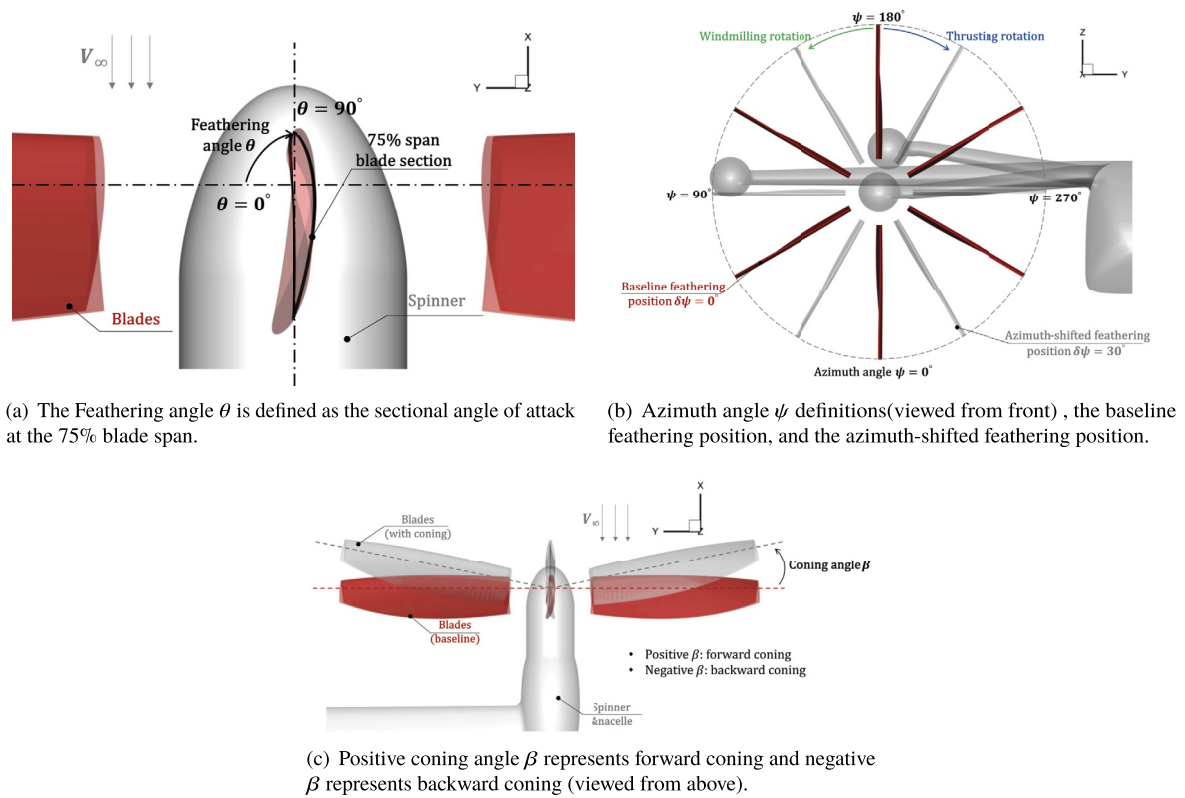
(a) The Feathering angle θ is defined as the sectional angle of attack at the 75% blade span.

(b) Azimuth angle ψ definitions(viewed from front) , the baseline feathering position, and the azimuth-shifted feathering position.

(c) Positive coning angle β represents forward coning and negative β represents backward coning (viewed from above).

Fig. 2. Definitions of the feathering angle θ, azimuth shift $\delta\psi$, and coning angle β for the investigation of feathered blades.

the loading distributions on downstream wings, and sectional flow solutions to understand the overall performance and interactions.

3. Numerical methods

3.1. HMB3 framework

High-fidelity CFD simulations in this work were carried out using the in-house Helicopter Multi-Block 3 (HMB3) [10,14] numerical framework. This well-established framework enables high-fidelity, multi-disciplinary modelling of general aerospace problems encompassing aerodynamics, acoustics, flight mechanics, and aero-elastics. For the aerodynamic modelling, the HMB3 flow solver solves the Unsteady Reynolds Averaged Navier-Stokes (URANS) equations in integral and Arbitrary Lagrangian Eulerian forms. The governing flow equations are discretised in space using cell-centred finite volume schemes on multi-block, fully structured grids as:

$$\frac{d}{dt}\left(\mathbf{W}_{i,j,k}A_{i,j,k}\right) = -\mathbf{R}_{i,j,k}\left(\mathbf{W}_{i,j,k}\right),\qquad(1)$$

where i,j,k represent the cell index, $\mathbf{W}$ and $\mathbf{R}$ are the vector of conservative flow variables and residual respectively, and $A_{i,j,k}$ is the volume. To evaluate the convective fluxes, Osher's approximate Rieman solver is used, while the viscous terms are discretized using a second order central difference scheme. The 3rd order MUSCL (Monotone Upstream-centered Schemes for Conservation Laws) approach was used to provide high-order accuracy in space. The chimera/overset grid method [15] was extensively used in this work. In the present work, simulations were performed with the $k-\omega$ SST [16] turbulence model. The temporal discretisation of Equation (1) uses fully implicit schemes.

The HMB3 solver has been extensively validated for the modelling of rotary-wings [17–19], propeller-wing interactions [13,20,21], and unconventional rotorcraft and eVTOL designs [10,22]. For this work, the modelling parameters, models, and grids are also inherited from our previous high-fidelity investigations of the Skybus concept [10,12].

The current study focused on the integrated aerodynamic loadings and flow solutions computed through HMB3. For visualisation, interpretation, and interpolation purposes, the Kriging model [23] was widely adopted to construct response surfaces of the loading results. This work adopted the Ordinary Kriging with a Gaussian kernel and a constant regression (the mean value) [23]. The stochastic parameters were determined using the maximum likelyhood estimation. These were realised using the open-source Surrogate Modelling Toolbox (SMT) [24].

3.2. Meshing and modelling details

To alleviate the geometric complexity and enable the modelling of moving parts e.g. blades, the chimera/overset grid approach [10,15] has been extensively used in this work. The overset topology is presented in Fig. 3. High-quality boundary layer meshes were individually generated for the airframe and for the blades with the assistance of an automatic meshing framework [25]. The automation framework generated separate high-quality multi-block structured grids for components such as the blades, refinement, and background, upon parametric and CAD inputs. The grids were then assembled with multi-block near-body refinement and background grids for the simulations. All boundary layer meshes were constructed with y+ = 1. When changing the blade feathering or coning angles, the blade grids were rotated as necessary, and were re-assembled for the new simulation. The grid spacing and cell counts remained constant for the study.

The component grid details are presented in Table 2. These were the same grids that have been used in our previous aerodynamic and acoustic modelling [10,12,26] of the Skybus concept, including a complete grid convergence study in Ref [26]. The airframe grid had minor modifications to remove refinement for the middle and aft propellers, which were excluded for the feathering blade analyses. The mesh size and spacing adopted recommendations from previous high-fidelity simulations of unconventional rotorcraft configurations [27–29]. The spacing of the airframe grid enclosing the propellers were between 0.035 to 0.15 of the blade 75% chord length. The near-body refinement had the
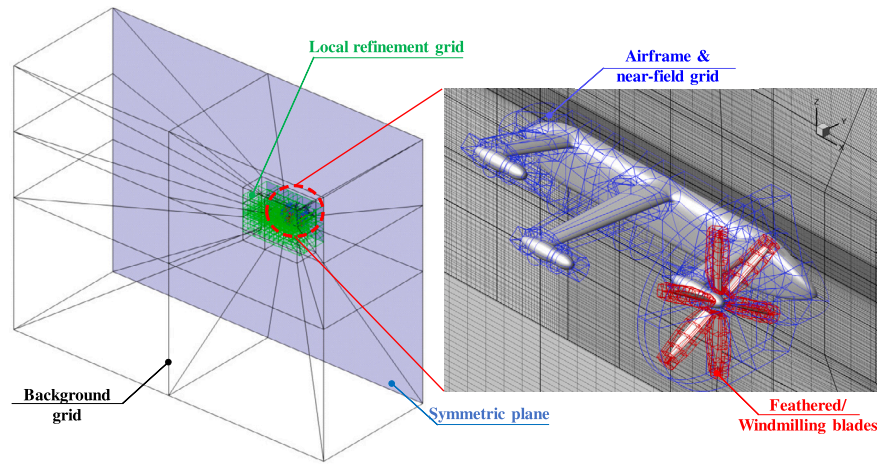
Fig. 3. Grid details and overset topology for simulations of the multi-rotor model with feathered/windmilling upstream blades.

Table 2
Component grid details for HMB3 simulations of the feathered and windmilling half-model (in million cells).

Blades	Airframe	Near-body refinement	Background	Total
1.3 per blade	31.2	16.1	0.9	56.0

spacing of 0.15 of the blade chord within 4 to 5 radii away from the vehicle. These were fine enough to resolve near-field acoustic solutions as in the previous study [10,26]. In total, 56 million cells were used for the half-model.

For this study, all simulations were performed at nominal cruise conditions 1000 metres above sea level. The free-stream velocity was 90 m/s with zero incidence or sideslip, resulting in a free-stream Mach number of 0.27. The reference density was 1.11 kg/m^3. The Reynolds number based on the free-stream and the blade radius was 1.8×10^7. Simulations of the feathered blades without moving parts were all assumed steady. For the simulations of the windmilling cases, regardless of the windmilling rotational speed, a time step of 1°/step for the rotation was adopted, considering that the axial speed was dominant in cruise.

4. Feathered propeller performance

This section evaluates the performance of feathered propellers, and their interference on downstream components (Cases 1, 2, 3 in Table 1). The study starts from the integrated aerodynamic loadings and evaluates the overall impact of the feathering angle θ, azimuth shift $\delta\psi$, and coning angle β. The investigation then moves to the detailed flow solutions to understand the aerodynamic interactions between the feathered blades and wings. Comparisons were made against the clean airframe to highlight the interferences.

Figs. 4(a) to 4(d) present representative HMB3 flow solutions for the clean airframe, for Cases 1, 2, and 3, respectively. The pressure coefficient contours are presented, and the transparent iso-surfaces corresponds dimensionless Q-criteria illustrating the wake systems of each aerodynamic components. The clean airframe solution in Fig. 4(a) was computed at the same free-stream speed of 90 m/s, with zero incidence and sideslip. This case was used to normalise further results, as a basis for comparisons, and to highlight interactional aerodynamics due to the redundant blades.

In general, with various arrangements for the redundant blades, the resolved flow solutions were largely similar to the basic clean airframe case, especially around the fuselage. Differences were concentrated near the wings, brought in by the different blade wake systems. The quan-

titative comparisons and correlations are detailed in the following subsections.

4.1. Overall loading variations

This section focuses on the integrated loading variations to quantify the effects of the feathering angle θ, azimuth shift $\delta\psi$, and cone angle β. The overall lift and drag variations due to blade feathering angle (θ) changes (Case 1) are shown in Figs. 5(a) and 5(b). Note that the lift and drag values have been normalised using the clean airframe (Fig. 4(a)) lift L_0 and drag D_0, respectively, to reflect the relative changes.

Simply changing the blade feathering had a substantial impact on the overall lift. As shown in Fig. 5(a), when increasing the feathering angle θ from 80 degrees to 100 degrees, the lift was reduced by about 25%. This was primarily associated with the lift loss of the airframe (wings and fuselage), as indicated by the dashed lines in Fig. 5(a). The propeller made a small contribution (about 0.02 L_0) to the overall lift, as shown by the differences between the overall and airframe lift. The lift change was due to the interference between the blades and the airframe, as discussed in later sections.

The feathered blades brought significant drag increases compared to the clean airframe, and the drag varied with the feathering angle. Fig. 5(b) shows that $\theta = 85°$ had the minimum overall drag of about 1.3 D_0, for the range investigated. At $\theta = 85°$, the airframe drag was almost the same as that of the clean airframe, and the propeller contributed the extra 0.3 D_0. When increasing the feathering angle from 85 to 100 degrees, the airframe drag was slightly reduced by about 0.2 D_0, but the propeller drag was substantially increased by about 0.7 D_0, hence the overall drag was increased by about 0.5D_0. Reducing θ from 85 to 80 degrees showed similar effects as increasing it to 90 degrees. At high feathering angles, the propeller drag was substantial, e.g. at $\theta = 100°$, the overall propeller drag was the same as the drag of the entire clean airframe.

Figs. 6(a) and 6(b) present the overall lift and drag changes for a 30-degree azimuth shift $\delta\psi$, for the feathered blades (Case 2). Compared to Case 1, the azimuth shift $\delta\psi$ brought limited overall lift and drag changes. The lift changes in Fig. 6(a) are negligible, and the overall drag was slightly reduced by 0.1 D_0 as shown in Fig. 6(b). This drag reduction was associated with the airframe due to blade interactions, at different azimuth positions, but the propeller drag remained the same despite the azimuth changes. These minor effects of the azimuth changes should be correlated with the high blade number (6), which evens the influences of the blades.

Figs. 7(a) and 7(b) present the overall lift and drag changes due to the cone angle, β, for the feathered blades at $\theta = 85°$ (Case 3). The overall lift and drag remained almost unchanged at small coning angles, despite the reducing disk radius. With these small coning angles,
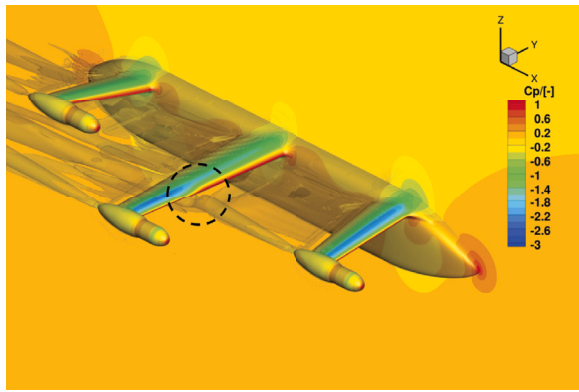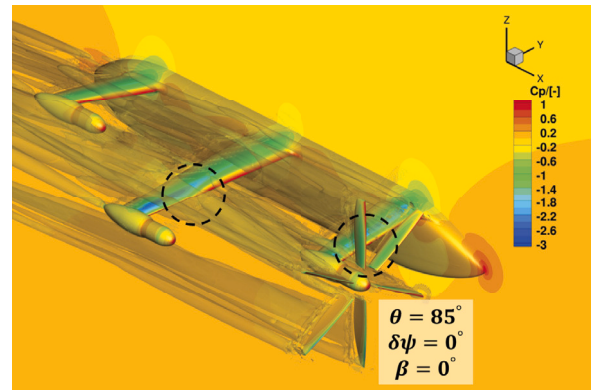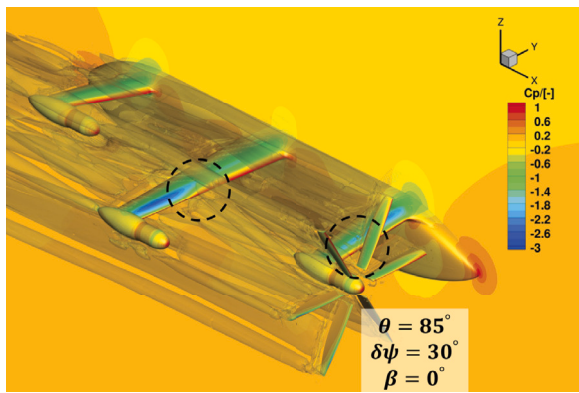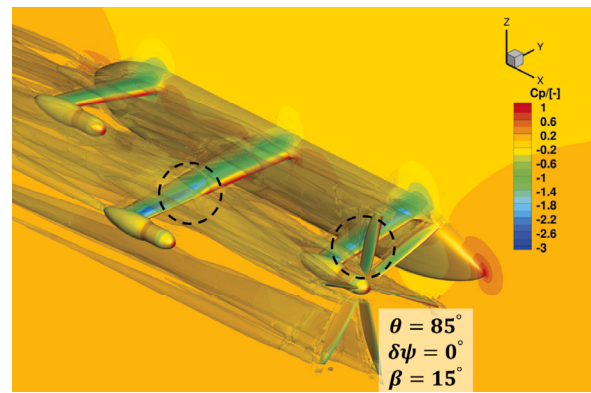
(a) Clean airframe without blades.

(b) Airframe with feathered blades at $\theta = 85°$, $\delta\psi = 0°$, and $\beta = 0°$ (Case1).

(c) Airframe with feathered blades at $\theta = 85°$, $\delta\psi = 30°$, and $\beta = 0°$ (Case2).

(d) Airframe with feathered blades at $\theta = 85°$, $\delta\psi = 0°$, and $\beta = 15°$ (Case3).

Fig. 4. Flow solutions of the airframe with and without feathered blades (Cases 1, 2, 3 in Table 1). The contours are pressure coefficients C_p, and the transparent iso-surfaces are dimensionless Q-criteria of 0.01 showing component wakes. (For interpretation of the colours in the figure(s), the reader is referred to the web version of this article.)

there were only minor changes in the overall projection area exposed to the free-stream, and there were also minor changes in the downstream interference as will be shown later. Larger coning angles are expected to have strong impacts, but this will lead to the mechanical complexity.

4.2. Component loading variations

This section presents the individual loading variations of the wings, fuselage, and blades to identify component contributions and variations, subject to feathering angle and azimuth shift changes. The airframe (i.e. wings and fuselage) lift and drag variations due to feathering angle changes (Case 1) are presented in Figs. 8(a) and 8(b). The shaded lines represent the corresponding clean airframe components to highlight the changes due to the feathered blades.

In terms of lift, Fig. 8(a) shows that the front wing suffered the most losses due to interference. When the feathering angle was increased from 80 degrees to 100 degrees, the front wing lift was reduced from 0.3 L_0 to 0.15 L_0, a significant reduction of 50%. This reduced wing lift, as will be detailed in later sections, was caused by the lifting propeller blades upstream the wing, which created a downwash and reduced the angle of attack. The middle wing, aft wing, and fuselage also experienced a minor lift loss of about 0.02 L_0 compared to the clean airframe case, following the feathering angle increases. For this configuration, the front wing was an important lift source, second only to the middle wing. Such significant lift loss, had a strong impact on the overall lift as shown in Fig. 5(a). Note that the fuselage also contributed to the lift because the wing roots were regarded as part of the fuselage, as shown in Fig. 1. Overall, the wing lift was negatively affected by the feathered blades, and the front wing suffered particular lift losses.

The drag variations in Fig. 8(b) show more complexities. It is first noted that the drag of the middle wing was substantially reduced compared to the clean airframe case, while the feathering angle was increased. From $\theta = 80°$ to $\theta = 100°$, its drag was reduced from 0.39 D_0 to 0.12 D_0, a 70% reduction. This is inconsistent with the almost constant lift in Fig. 8(a), suggesting local aerodynamic interference, which will be investigated in later sections.

Meanwhile, the drag of the front wing increased compared to the clean airframe. As the feathering angle was increased, the drag increased from 0.23 D_0, to a peak value of 0.29 D_0, at $\theta = 90°$ and $\theta = 95°$, then slightly decreased to 0.27 D_0 at $\theta = 100°$. The aft wing and fuselage drag remained almost constant. Together with the decreased middle wing drag, the overall airframe drag forces were slightly reduced as shown in Fig. 5(b). However, the overall drag was still increased due to the growing feathered propeller drag.

The single-blade drag variations at different feathering angles and azimuth shifts are presented in Fig. 9. The scatters in Fig. 9 denote the sampling points (taken from Cases 1 and 2) for the curve fitting.

For this six-bladed propeller, the drag of each blade was almost the same when they had the same feathering angle, despite the azimuth difference. This is reflected by the concentric pattern around the azimuth in most areas of Fig. 9. The single-blade drag had a minimum at about $\theta = 85°$, and otherwise grew with increasing or decreasing feathering angles. The drag was particularly high at high feathering angles for the range investigated.
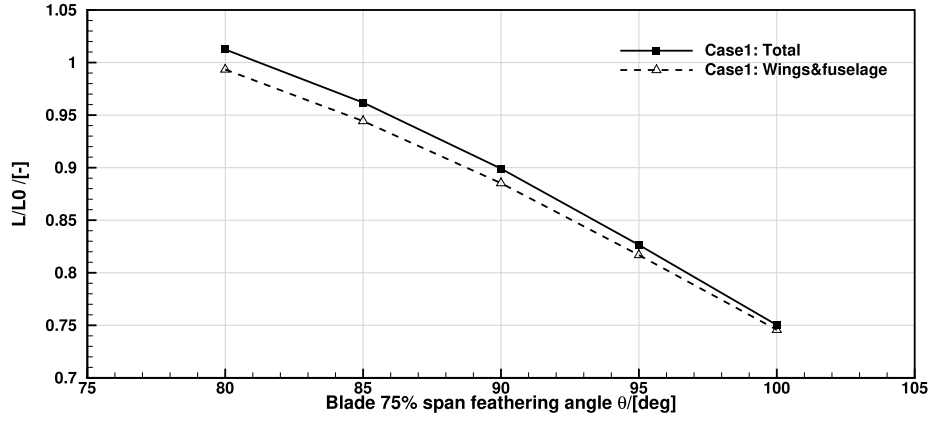
(a) Overall lift variations (normalised with clean airframe lift L_0).
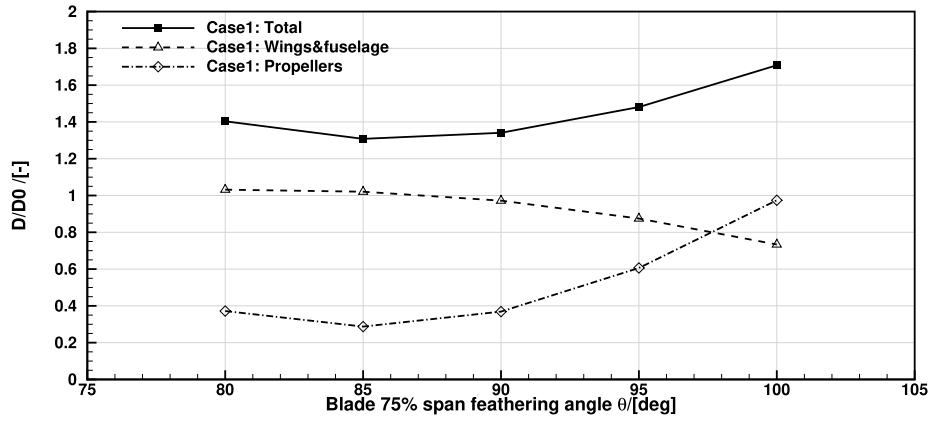
(b) Overall drag variations (normalised with clean airframe drag D_0).

Fig. 5. Overall lift and drag variations following feathering angle changes (θ), Case 1 of Table 1.

However, between 210-degree and 300-degree azimuth angles, the feathered blades showed particularly low drag compared to other azimuth positions. This is associated with aerodynamic interactions with the airframe, especially with the front wing at these azimuth positions. The detailed interactions are discussed in the next section.

5. Aerodynamic interference of the feathered blades

It has been shown in previous sections that the aerodynamic impact of feathering is mostly on the front and middle wings. For the front wing, the main impact was a substantial loss of lift, as the blade feathering angle increased. For the middle wing, the major impact is a drop of drag while the lift stayed almost constant. This subsection investigates the underlying flow physics. The study will start from the wing loading distributions, and will focus on the wing sectional aerodynamics. As shown in Figs. 10(a) and 10(b), the flow solutions were sliced and probed at several spanwise stations, to inspect the sectional aerodynamics for the front and middle wings. For the front wing, these were the 40%, 60%, and 80% spanwise sections. For the middle wing, these were the 25%, 50%, and 75% sections of the span.

It will be shown later that the induced flow of the feathered blades altered the local Angle of Attack (AoA) of the downstream wing sections. This was due to changes of the local flow conditions, but the lift and drag decomposition had to follow the free-stream. This is illustrated in Figs. 11(a) and 11(b), where L_w and D_w are the sectional lift and drag following the local AoA. The sectional lift L and drag D in the body or global axis can be written as:

$$L = L_w cos(\delta\alpha) + D_w sin(\delta\alpha)$$
$$D = -L_w sin(\delta\alpha) + D_w cos(\delta\alpha) \tag{2}$$

where $\delta\alpha$ is the sectional AoA change. $L_w = L_w(\alpha + \delta\alpha)$ and $D_w = D_w(\alpha + \delta\alpha)$ are of course functions of the AoA changes, and can be regarded as monotonic linear functions within the typical operation range. With zero AoA change, L_w and D_w coincide with L and D. If we assume that $\delta\alpha$ is a small value close to zero, Equation (2) can be approximated by taking $cos(\delta\alpha) \approx 1$ and $sin(\delta\alpha) \approx \delta\alpha$:

$$L \approx L_w + D_w\delta\alpha$$
$$D \approx -L_w\delta\alpha + D_w \tag{3}$$

With small positive local AoA changes in Fig. 11(a), i.e. $\delta\alpha > 0$, both L_w and D_w would increase. From Equation (3) and this leads to increased total L and reduced total D. If L_w is much larger than D_w (high lift-to-drag ratio), the net drag could even become negative (forward suction force), due to the strong lift-induced contribution opposite to the drag direction. This of course depends on the sectional aerodynamic characteristics and flow conditions.

On the other hand, when the local AoA change is negative as shown in Fig. 11(b), i.e. $\delta\alpha < 0$, both L_w and D_w would decrease. This leads to decreased total L, while the drag D changes may vary. The strong lift-induced contribution is now aligned with the drag direction. If there is a small drop in the lift and the sectional lift-to-drag ratio is high, the drag should increase. However, if the lift drop is substantial and the sectional lift-to-drag ratio is low, then the drag may decrease. The
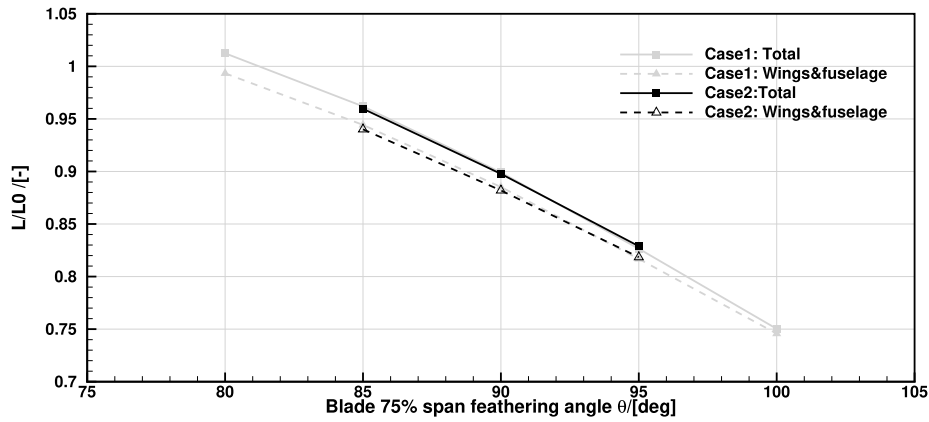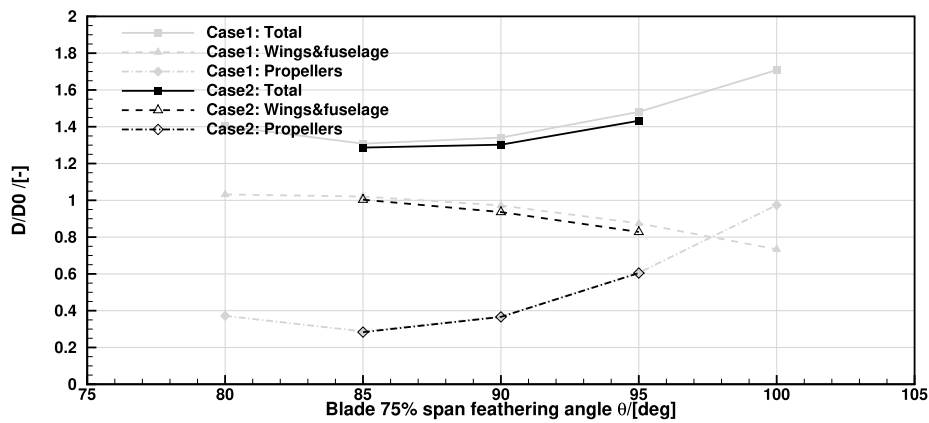
(a) Overall lift variations (normalised with clean airframe lift L_0).

(b) Overall drag variations (normalised with clean airframe drag D_0).

Fig. 6. Overall lift and drag variations with following feathering angle changes (θ) with a 30 degree azimuth shift ($\delta\psi$), Case 2 of Table 1. The shaded lines are corresponding results of Case 1 to highlight the comparisons.

following analyses of the flow solutions will follow these lift and drag decomposition discussed here.

It must be stressed that this is a simplified approach to help us understand the complex aerodynamic interactions. We have neglected changes in the local flow speed and 3D effects. It is also hard to find the exact local AoA and AoA changes directly from the flow solutions. Nevertheless, this simple analysis reflects well the primary aerodynamic impacts due to the inflow angle changes, and shows good correlations with the high-fidelity yet complex CFD results.

5.1. Aerodynamic interference on the front wing

5.1.1. Sectional aerodynamics and influence of blade feathering angle

The sectional aerodynamic performance analyses focus on the pressure (Cp contours) and the velocity fields. Figs. 12(a) to 12(c) present the flow solutions through the 40%, 60%, and 80% spanwise sections of the front wing. Flow fields of the clean airframe (Fig. 4(a)) are shown in Fig. 12(a). Without the blades, these front-wing sections were simply exposed to the clean free-stream.

Solutions of Case 1 with $\theta = 85°$, $\delta\psi = 0°$, and $\beta = 0°$ are presented in Fig. 12(b). At the inner section of $y/b_a = 0.4$, the flow field remained similar to the clean airframe (Fig. 12(a)), since this section is out of the blade radius with $\delta\psi = 0°$. At sections of $y/b_a = 0.6$ and $y/b_a = 0.8$, the upstream blades affected the inflow of the downstream wing, thereby changing the sectional effective angle of attack and consequently the sectional performance. When the feathered blades induced a considerable downwards velocity, reducing the local flow angle of the down-

stream front wing, significant lift loss can be noted in the wing loading (Figs. 13(a), 13(b), and 8(a)).

The impact of the feathering angle is further evaluated with Fig. 12(c) with the feathering angle increased to 95 degrees. At the sections of $y/b_a = 0.6$ and $y/b_a = 0.8$, the blades directed the velocity further downwards, reducing the local flow angles of the downstream front wing, leading to reduced front wing lift. This is reflected in the smaller pressure differences over the wing upper and lower surfaces, and is consistent with the lift decrease with growing feathering angle in Fig. 8(a). The front-wing drag, however, as shown in Fig. 8(b), was only slightly increased. This was due to the reduced lift causing lower lift-induced drag. The inner section of $y/b_a = 0.4$ in Fig. 12(c) is still similar to the clean airframe since it was outside the rotor disk.

5.1.2. Front wing loading distributions subject to feathering angle changes

The front wing lift and drag pressure loading distributions were extracted and presented in Figs. 13(a) and 13(b), to have an overview of the interference subject to blade feathering angle changes (Case 1). In general, as the blade feathering angle was increased, the front wing lift was reduced at stations along its span. This is consistent with the significant overall lift loss in Fig. 8(a). The drag was generally increased along the span as the feathering angle increased, but near the sections of $y/b_a = 0.7$ and $y/b_a = 0.8$, the sectional drag was reduced for feathering angles beyond 90 degrees. This drop of the drag was caused by the reduced lift-induced drag (Fig. 11(b)), as the lift was significantly decreased.
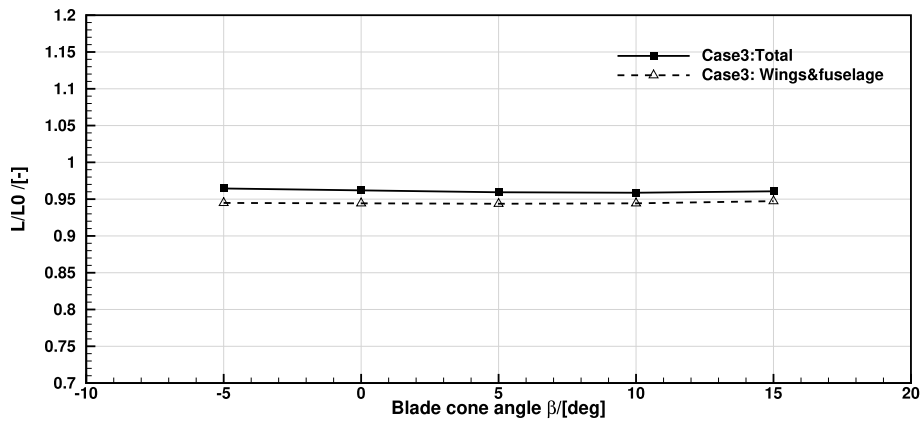
(a) Overall lift variations (normalised with clean airframe lift L_0).
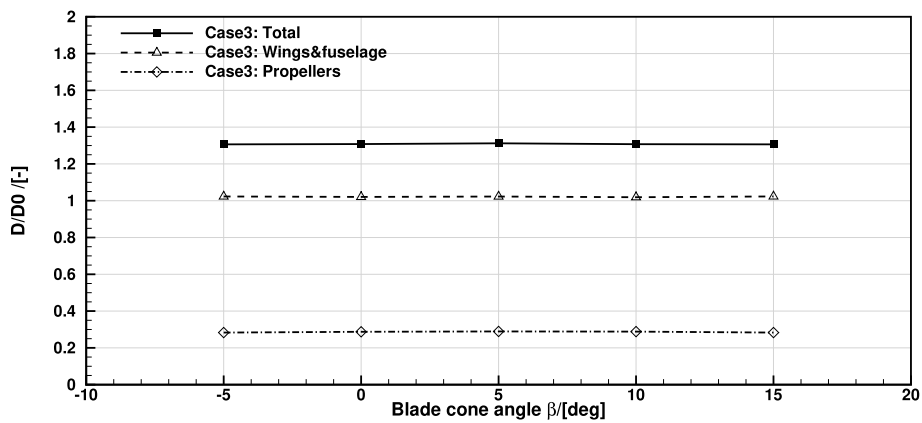
(b) Overall drag variations (normalised with clean airframe drag D_0).

Fig. 7. Overall lift and drag variations with following cone angle changes (β) at $\theta = 85°$, Case 3 of Table 1.

Overall, the lift/drag distributions of the front wing subject to feather angle changes correlate well with the situation illustrated in Fig. 11(b). This suggests that the feathered blades mostly caused negative local flow angle changes to the front wing.

5.1.3. Influence of azimuth shift and coning

The influence of azimuth shift (Case 2) on the front wing is investigated in Fig. 14(a). With the 30-degree azimuth shift, the $y/b_a = 0.4$ section was also exposed to the blade wake, as shown in Fig. 14(a). Nonetheless, the feathered blades had similar effects despite the azimuth shift, i.e. changing the sectional velocities according to the local blade camber and feathering angle. At the inner section in Fig. 14(a), the blade actually increased the local flow angle of the front wing, due to the negative blade pitch angle, as per the blade twist. As the feathering angle θ was increased, the flow was deflected further downwards, and the local flow angle of the front wing was further reduced. These resulted in the lift loss shown in Fig. 6(a), which is similar to that of Case 1 of Fig. 5(a). Note that the azimuth shift is also associated with the high blade count of the current propeller, which is promoting axial symmetry, diminishing the differences.

The influence of the coning angles β (Case 3) is shown in Fig. 14(b) (with $\theta = 85°$, $\delta\psi = 0°$, and $\beta = 15°$). The positive coning (Fig. 2(c)) slightly moved the blade tip sections away, by about one chord length from the front wing. For section $y/b_a = 0.8$ which is close to the blade root, the coning only moved the blade sections by about half a chord length since they are closer to the coning centre. Nonetheless, the blades still redirected the inflow for the downstream wing, and the slightly in-

creased stream-wise distance resulted in minor differences compared to the non-coning Case 1. This led to the negligible changes shown in Figs. 7(a) and 7(b) for small coning angles. However, it should be highlighted that substantial changes in the coning angle, i.e. folding the blades (either backwards or forwards), should have a major impacts by reducing the interactions.

These pressure fields also explain the reduced blade drag near $\psi = 210°$ and $\psi = 300°$ in Fig. 9. As can be noted in Figs. 12(b) and 12(c), the blades benefit from the stagnation areas of the front wing when placed nearby. This higher pressure near the trailing edge counters the stagnation pressure near the blade leading edge, thereby reducing the blade drag. This is the wing's upstream interference on the blades through the pressure field, but the wing drag was slightly increased since the interaction is mutual. When the blades were placed elsewhere, this phenomenon was not present, and the blades had almost the same drag properties regardless of the azimuth.

5.2. Aerodynamic interference on the middle wing

5.2.1. Influence of blade feathering angle

Sectional flow solutions were extracted at the 25%, 50%, and 75% spanwise locations of the middle wing, as shown in Fig. 10(b). The basic clean airframe solution is presented in Fig. 15(a). Even without the blades, the middle wing has already been affected by the front wing. As shown in Fig. 15(a) at $y/b_m = 0.25$ and $y/b_m = 0.5$, the front wing deflected the inflow downwards due to its own loading, thereby decreasing the effective angle of attack for the downstream middle wing
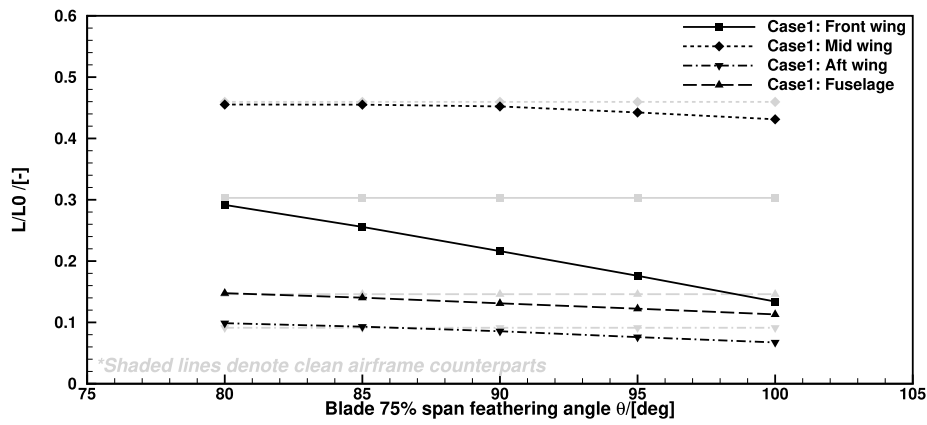
(a) Lift variations (normalised with clean airframe lift L_0).
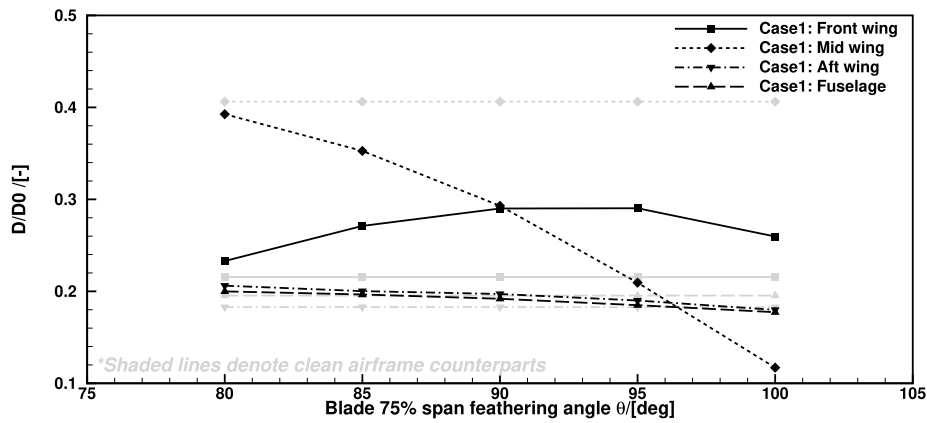
(b) Drag variations (normalised with clean airframe drag D_0).

Fig. 8. Airframe lift and drag variations following feathering angle changes, Case 1 of Table 1. The shaded horizontal lines denote the corresponding component lift and drag values of the clean airframe.
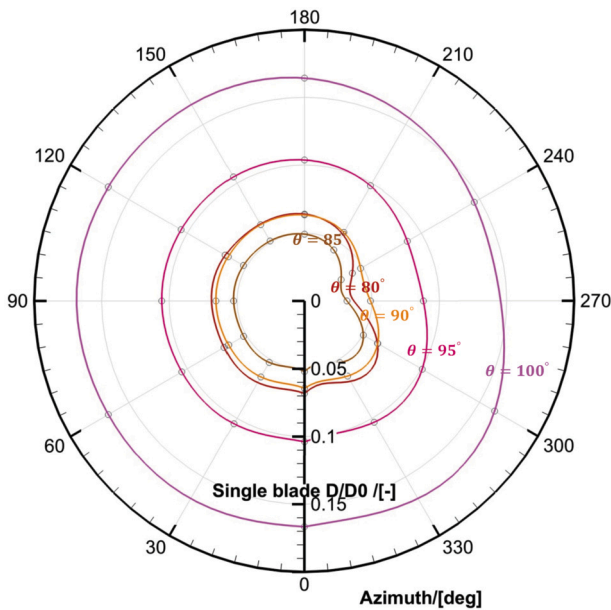

Fig. 9. Single blade drag variations at different feathering (θ) and azimuth (β) angles (the scatters denote sampling points).

sections. At $y/b_m = 0.75$, however, due to the wing tip vortex of the front wing, an upward flow was seen in that section.

When the feathered blades were added as shown in Fig. 15(b) for Case 1, $\theta = 85°$, $\delta\psi = 0°$, $\beta = 0°$, further interference occurred above the existing wing-wing interactions. The inner section of $y/b_m = 0.25$ remained similar to the clean airframe, since it is outside the blade radius with $\delta\psi = 0°$. For the mid-span section of $y/b_m = 0.5$, the feathered blades induced downwards velocities that affected the middle wing, thereby reducing the local flow angle at the sections compared to the clean airframe. According to Fig. 11(b), this led to decreased lift and slightly increased drag forces.

The outer section of $y/b_m = 0.75$ saw an increase of local AoA. This wing section was exposed to the outer part of the propeller blades, where the sectional camber was inverted compared to the inner blades. This inverse camber deflected the flow upwards, and the induced flow was free from the front wing, thereby increasing the effective attack angle for the middle wing. Following Fig. 11(a), this led to increased lift and reduced drag. Overall, this resulted in the substantial drag reduction in Fig. 8(b).

The influence of blade feathering angles is inspected in Fig. 15(c) with $\theta = 95°$. With this 10-degree increase in the feathering angle, the wing mid-span section's angle of attack was further reduced. The outspan section's attack angle was considerably increased, and a strong suction peak can be noticed near the leading edge of the section, which contributed to further reduced drag. These are consistent with the drag decrease with growing blade feathering angle in Fig. 8(b).
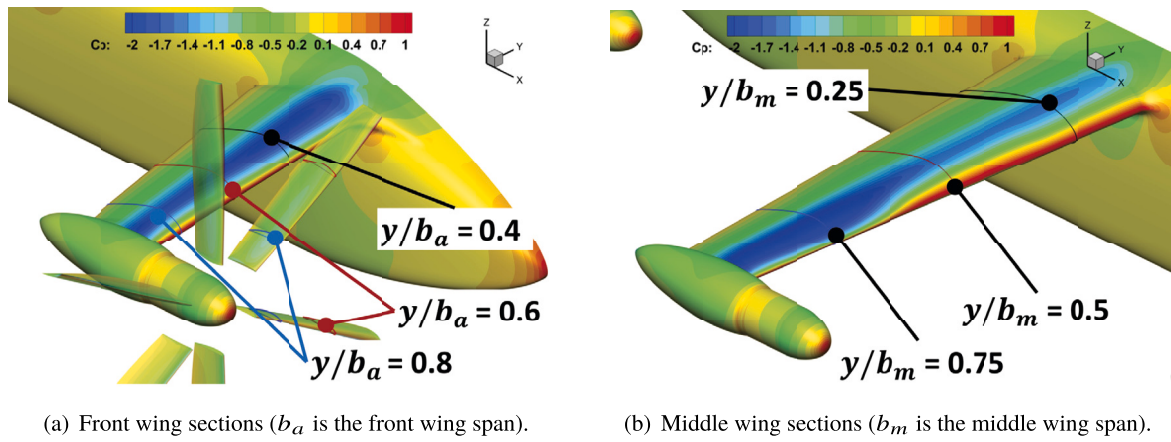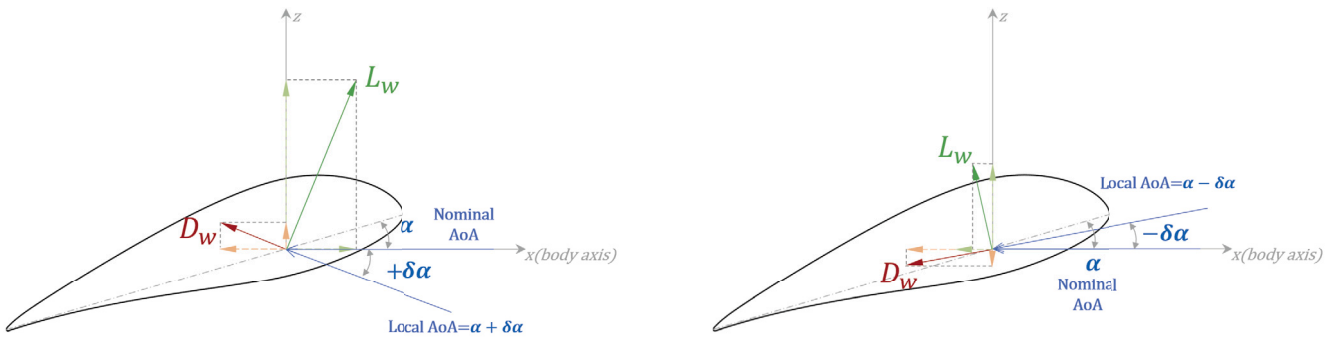
(a) Front wing sections (b_a is the front wing span).

(b) Middle wing sections (b_m is the middle wing span).

Fig. 10. Spanwise sections investigated for local flow interferences.

(a) Sectional loading decomposition with positive local angle of attack changes.

(b) Sectional loading decomposition with negative local angle of attack changes.

Fig. 11. Decomposition of sectional lift and drag from wind axis to body axis due to local angle of attack changes.

5.2.2. Middle wing loading distributions subject to feathering angle changes

This subsection elaborates the aerodynamic interference on the middle wing. For the middle wing, the main impact of the feathered blades was a significant drop of drag without losing much lift (Fig. 8(b)). The middle wing lift and drag distributions subject to feathering angle changes (Case 1) were extracted and presented in Figs. 16(a) and 16(b). The middle wing was subject to both positive and negative local changes as illustrated in Figs. 11(a) and 11(b).

For the clean airframe, the middle wing was already subject to the influence of the front wing, resulting in decreased lift and increased drag on the inner span, and increased lift and decreased drag on the outer span. The outer span benefits were due to the upwards flow induced by the front wing tip vortex, which slightly increased the local angle of attack. With the feathered blades and as the feathering angle was increased, the lift (Fig. 16(a)) was further decreased on the inner span of the wing where $y/b_m < 0.6$, and was increased on the outer span. The lift increase and decrease cancelled out each other and lead to almost constant overall lift as shown in Fig. 8(a).

In Fig. 16(b), the drag was substantially reduced on the outer wing sections, and became forward suction at high feathering angles. This can be correlated with the loading decomposition with positive AoA changes. Note that this was the pressure contribution and the viscous part always contributed to net drag forces. The tip nacelle also contributed to drag forces, and the overall drag force of the middle wing was still positive.

For the inner sections, where $y/b_m < 0.6$, the drag forces varied slightly, and some reductions were noted. This correlates well with the negative incidence changes in Fig. 11(b), and the reduced drag was be-

cause of the reduced lift-induced contributions. The overall result was consistent with the substantial drag reduction in Fig. 8(b).

5.2.3. Influence of azimuth shift and coning

The influence of azimuth shift (Case 2, $\delta\psi = 30°$) is investigated in Fig. 17(a). With the 30-degree azimuth shift, the inner middle wing section of $y/b_m = 0.25$ in Fig. 17(a) was also exposed to the blade wake, but the impact was weaker since the blade wake first interacted with the front wing. For the mid-span section, the angle of attack was reduced due to the downward deflected flow. For the outer span, the sectional angle of attack was increased due to the upward deflected flow. As the feathering angle was increased, these phenomena remained largely similar except that the flow angle was further increased/decreased accordingly. Overall, the azimuth shift showed small impacts on the middle wing performance due to the high blade number, which is consistent with the front wing angle in the previous section.

The influence of cone angle β (Case 3) is shown in Fig. 17(b) (with $\theta = 85°$, $\delta\psi = 0°$, and $\beta = 15°$). With this small 15-degree coning angle, the displacement of the blade sections due to the coning was minor compared to their original distance to the middle wing, hence the impact was minor. This is consistent with the integrated loading variations in Figs. 7(a) and 7(b). With higher coning angles towards folded blades, the impact should grow, as eventually only the wing tip will be exposed to the interactions.

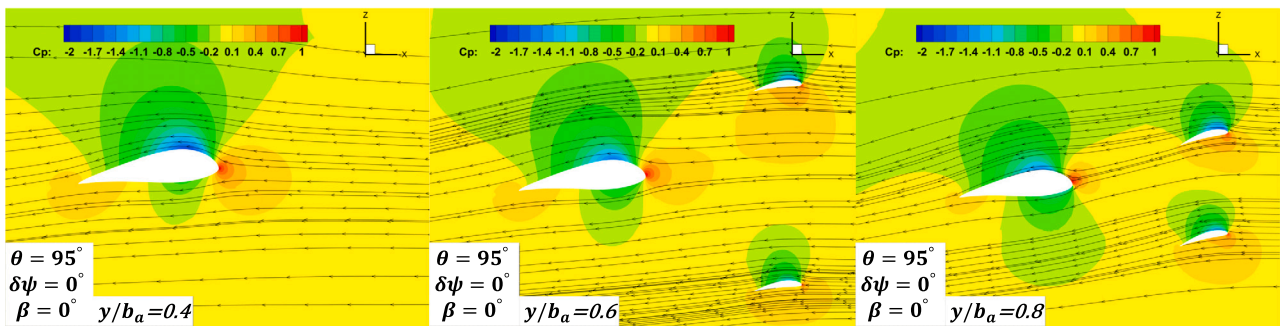## 6. Windmilling propeller performance

This section focuses on the aerodynamic performance of windmilling front propellers (Case 4 of Table 1). Figs. 18(a) and 18(b) present the
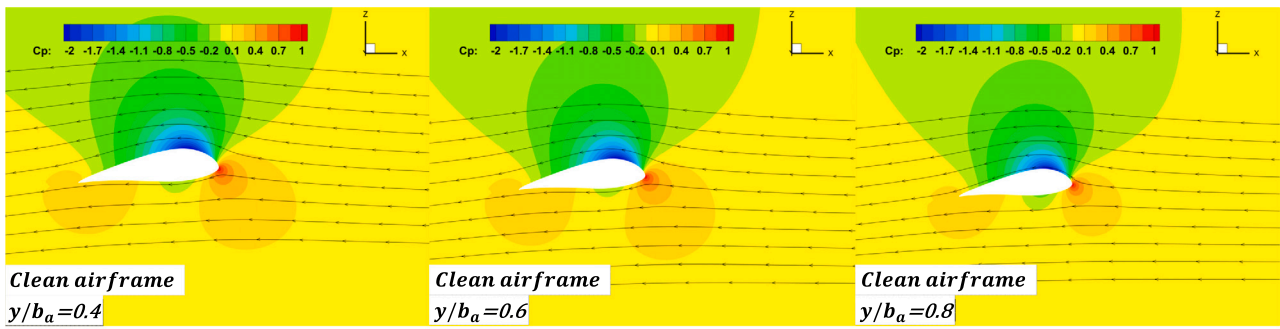
(a) Clean airframe.
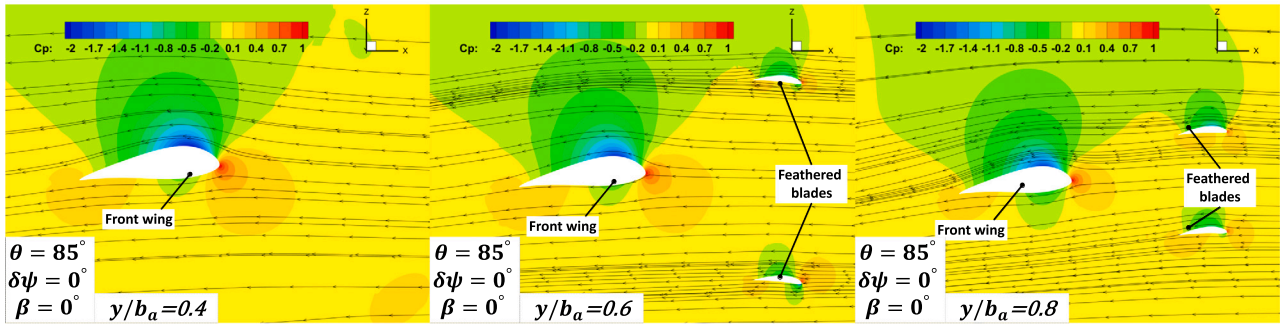
(b) Case 1, $\theta = 85°$, $\delta\psi = 0°$, $\beta = 0°$.

(c) Case 1 at higher feathering angle, $\theta = 95°$, $\delta\psi = 0°$, $\beta = 0°$.

Fig. 12. Comparisons of pressure coefficients and tangential streamlines at the 40%, 60%, and 80% spanwise sections of the front wing (clean airframe, and Case 1 results).

HMB3 flow solutions at two different feathering angles and windmilling speeds. Compared to the static feathered solutions in Figs. 4(b) to 4(c), the major difference is that the front propeller now creates a helical wake that dynamically hits the downstream wings. The strength and helicity of the wake depend on the rotational speed and feathering angle of the blades.

Note that in this windmilling performance analysis, the axial torque was assumed variable, where the extracted power might be positive (energy extraction) or negative (energy consumption). The propeller was allowed to rotate freely over a wide range of feathering angles, and rotational speeds, to understand how the windmilling performance and the overall performance would change.

6.1. Time-averaged aerodynamic loadings

This section discusses the time-averaged aerodynamic performance at different propeller feathering angles and rotational speeds. The propeller windmilling performance, in terms of drag and power extraction, is presented in Fig. 19(a) and 19(b), respectively. These are Kriging approximations constructed upon the sampling points represented by the dots. The drag values were normalised using D_0. The power values

were normalised using the required cruise power for the clean airframe, defined as $P_0 = D_0 V_\infty$.

The propeller drag in Fig. 19(a) closely followed the trend of the overall drag in Fig. 20(b), and the propeller drag values were approximately the total drag minus the clean airframe drag D_0. Compared to the feathered blades shown in Fig. 6(b), the windmilling drag was only slightly higher by about 0.1 to 0.2 D_0.

The extraction of wind energy in Fig. 19(b) is the major benefit of windmilling propellers. However, the propeller was only able to extract energy at certain combinations of feathering angles and RPM, as denoted by the solid lines in the right lower half in Fig. 19(b). Otherwise, the propeller needed energy to maintain its rotation, as shown by the dashed lines in the left upper half in Fig. 19(b). The current propeller design required energy input at low θ and high RPM. This is reasonable as lower feathering angles did not produce enough in-plane forces driving high-speed rotation.

The maximum power extraction is at $\theta = 100°$ and $RPM = 60$ for the range investigated. The propeller was able to extract 0.5 P_0 from the free-stream (assuming zero transmission/conversion loss and an adequate axial torque). However, this was realised at a cost since the
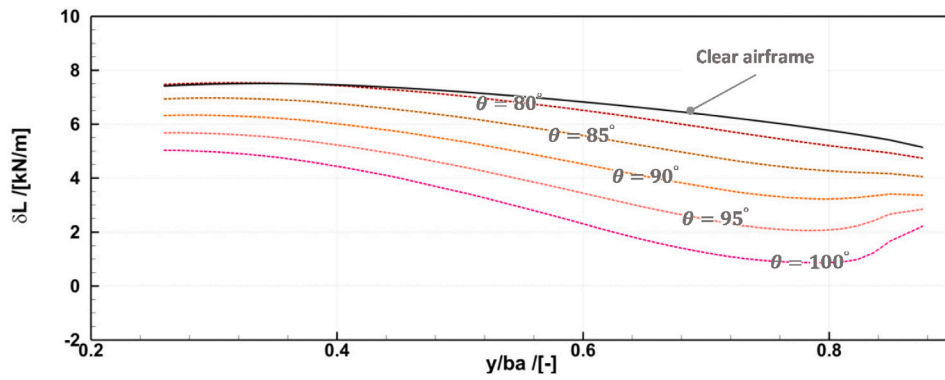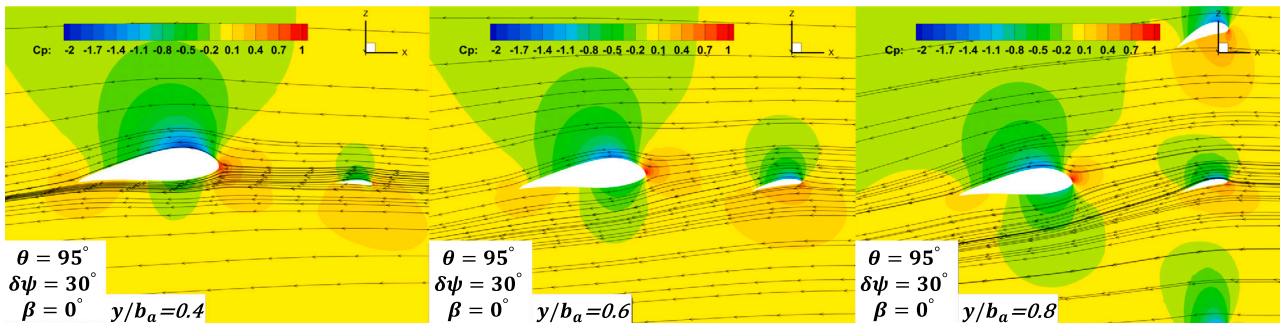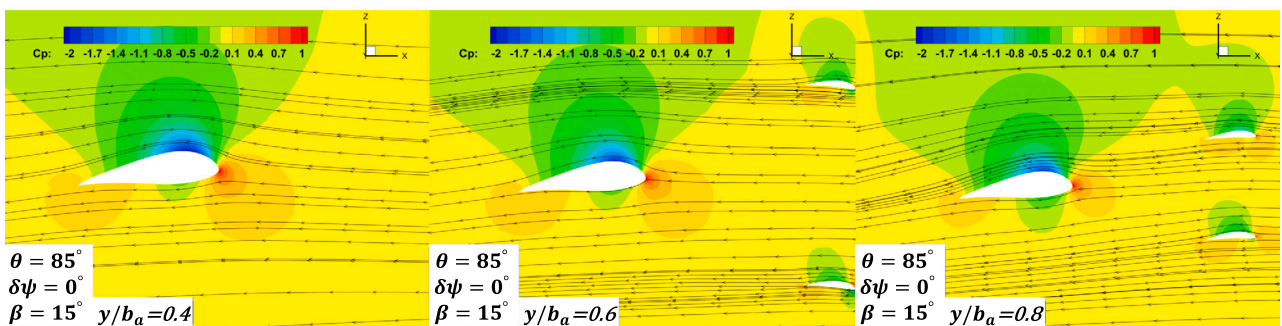
(a) Front wing lift loading.
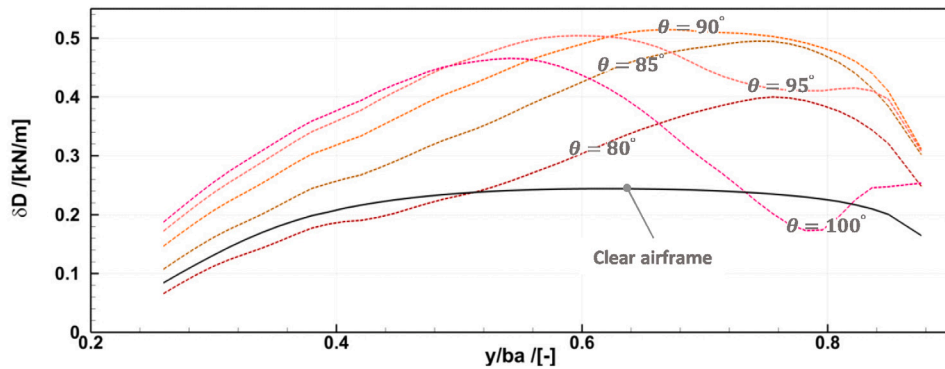
(b) Front wing drag loading.

Fig. 13. Front wing pressure loading distributions along the wing span subject to feathered blade interferences (Case 1).
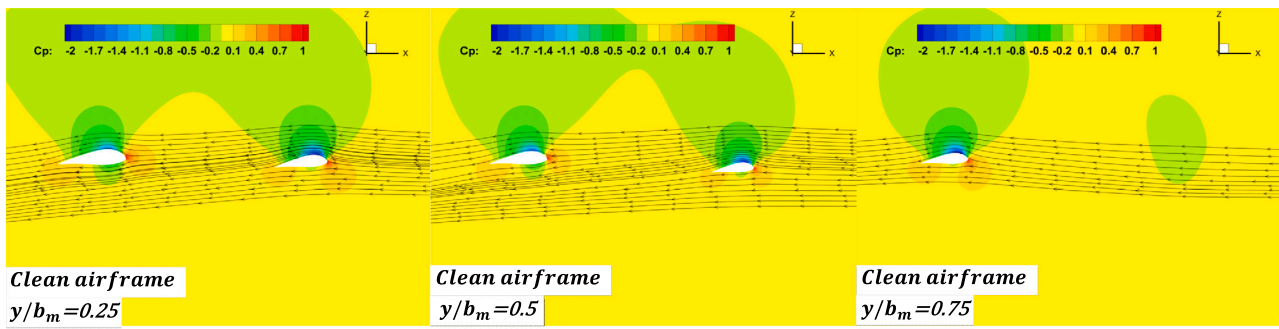

(a) Case 2 with azimuth shift changes, $\theta = 95°$, $\delta\psi = 30°$, $\beta = 0°$.

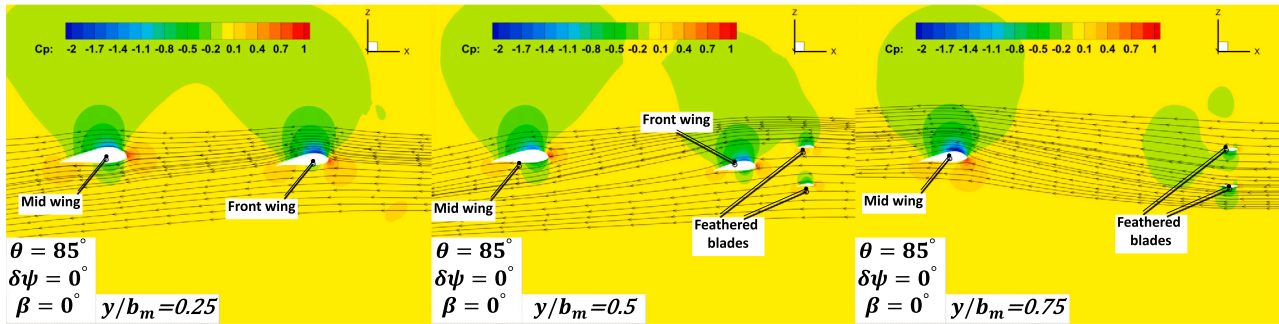(b) Case 3 with coning angle changes, $\theta = 85°$, $\delta\psi = 0°$, $\beta = 15°$, section $y/b_a = 0.4$.
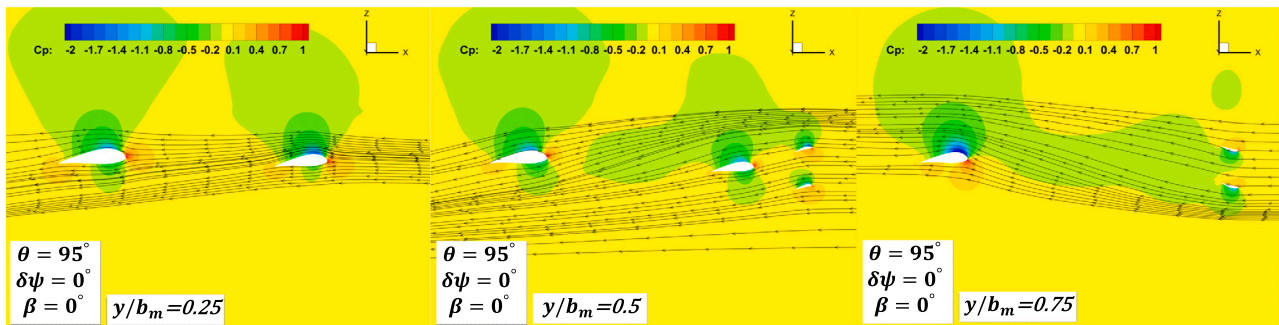
Fig. 14. Comparisons of pressure coefficients and tangential streamlines at the 40%, 60%, and 80% spanwise sections of the front wing (Cases 2 and 3).

(a) Clean airframe.

(b) Case 1, $\theta = 85°$, $\delta\psi = 0°$, $\beta = 0°$.

(c) Case 1 at higher feather angle, $\theta = 95°$, $\delta\psi = 0°$, $\beta = 0°$.

Fig. 15. Comparisons of pressure coefficients and tangential streamlines at the 25%, 50%, and 75% spanwise sections of the middle wing (clean airframe, and Case 1 results).

overall drag increased to about 1.9 D_0. The required cruise power in this case would be 1.4 P_0 $(1.9 - 0.5)$. Note that this is very similar to the required cruise power of 1.3 P_0, with the blade statically feathered at 85 degrees (Case 1 in Fig. 5(b)).

The overall lift and drag variations are presented in Figs. 20(a) and 20(b). These are also Kriging approximations taking θ and RPM as input, with the dots in the figures denoting the sampling points. The feathering angle ranged from 85 to 100 degrees, and the RPM ranged from 0 to 120. The lift and drag values were normalised using the clean airframe lift L_0 and drag D_0 to highlight the relative changes.

The total lift in Fig. 20(a) mostly followed diagonal variations, with higher lift at low feathering angles and high RPM, and lower lift at high feathering angles and low RPM. The highest lift was about 1.1 L_0 and the lowest lift was about 0.7L_0. There were some complications with medium θ and RPM combinations near the centre of the graph, but the lift variations were, in general, minor in this region. The propeller made minor lift contributions, hence the lift changes were again associated with the airframe subject to interference.

The total drag variations in Fig. 20(b) are more complex. Beyond $\theta = 95°$, the drag was dominated by the feathering angle, and had little dependence on the RPM. From $\theta = 95°$ to $\theta = 100°$, the overall drag was quickly increased from 1.5 D_0 to about 1.9 D_0. Below $\theta = 95°$, the overall drag showed more relevance to the RPM, but the variations were small. For the RPM range studied, the drag showed a minimum of about 1.3 D_0 at low and high RPM, and a maximum of about 1.5 D_0 near RPM 70 and 80.

These suggest that the windmilling option might be competitive compared to the feathering option, given that the extra drag and energy extraction are carefully balanced. Another benefit is that the windmilling blades decelerate the air flow, thereby creating a more favourable inflow condition for downstream thrusting propellers. The downstream propeller could also benefit from swirl recovery given the opposite rotational directions. These make the windmilling possibly a better option than feathering the blades. The next section will compare the windmilling and feathering performance for a complete cruise configuration.
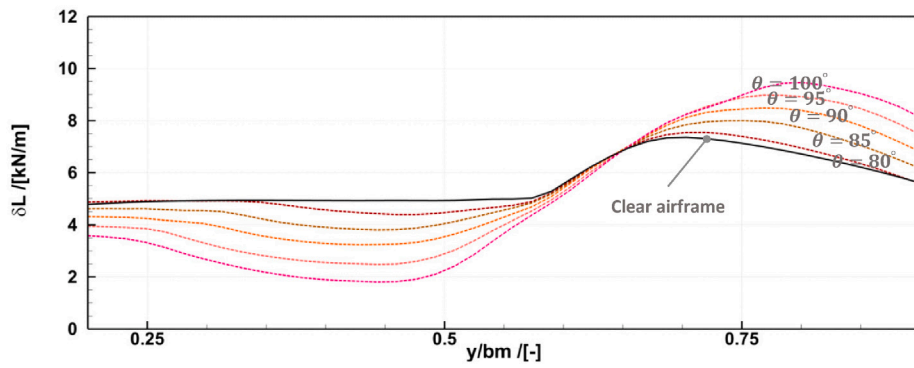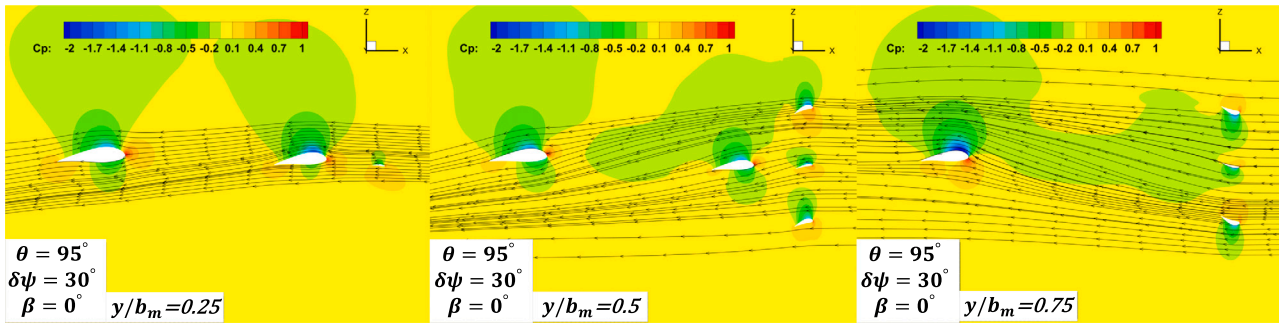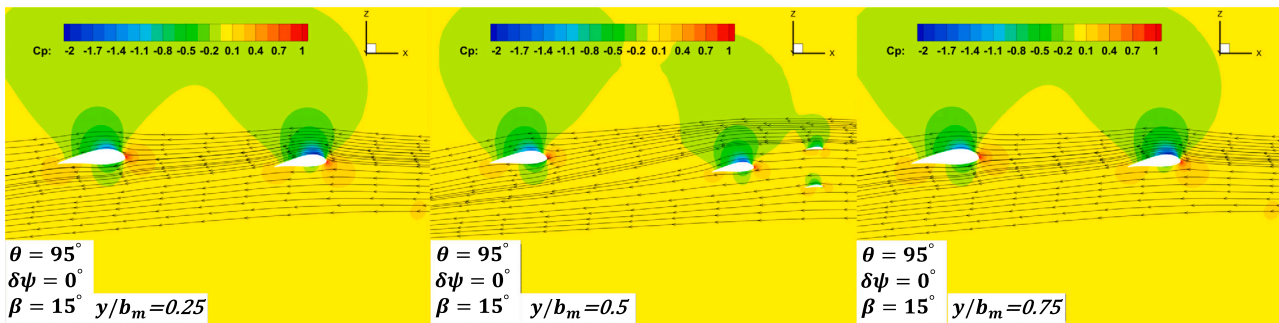
(a) Middle wing lift loading.
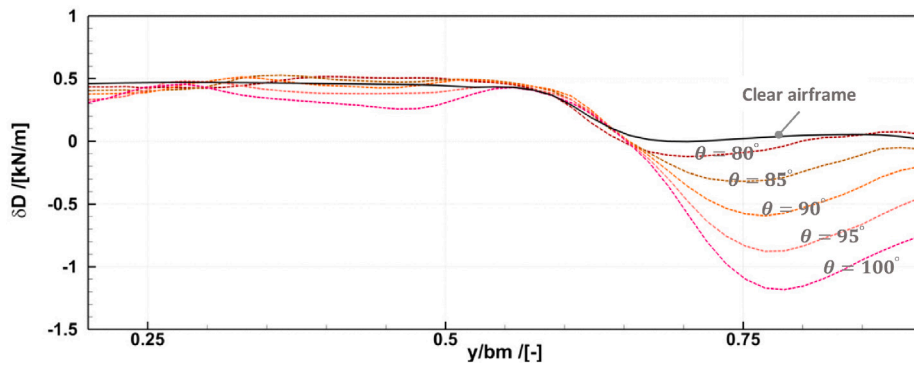
(b) Middle wing drag loading.

Fig. 16. Middle wing pressure loading distributions along the wing span subject to feathered blade interferences (Case 1).
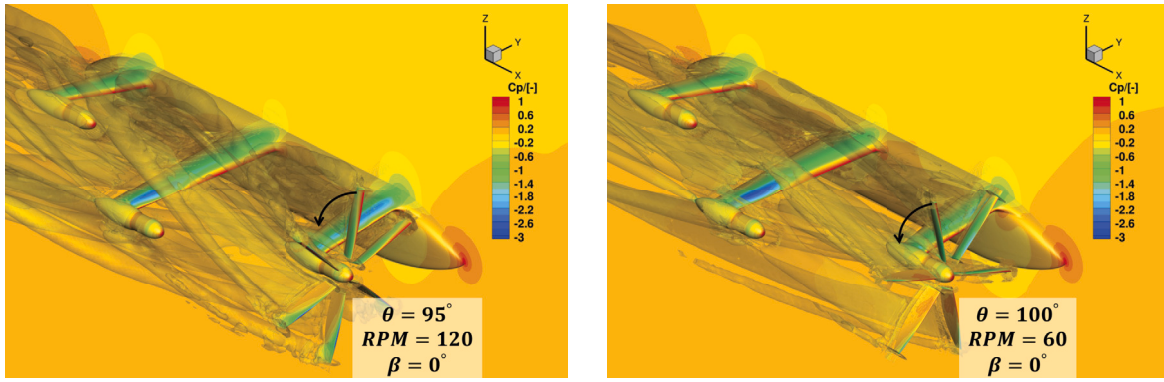

(a) Case 2 with azimuth shift changes, $\theta = 95°$, $\delta\psi = 30°$, $\beta = 0°$, section $y/b_m = 0.25$.

(b) Case 3 with coning angle, $\theta = 85°$, $\delta\psi = 0°$, $\beta = 15°$.
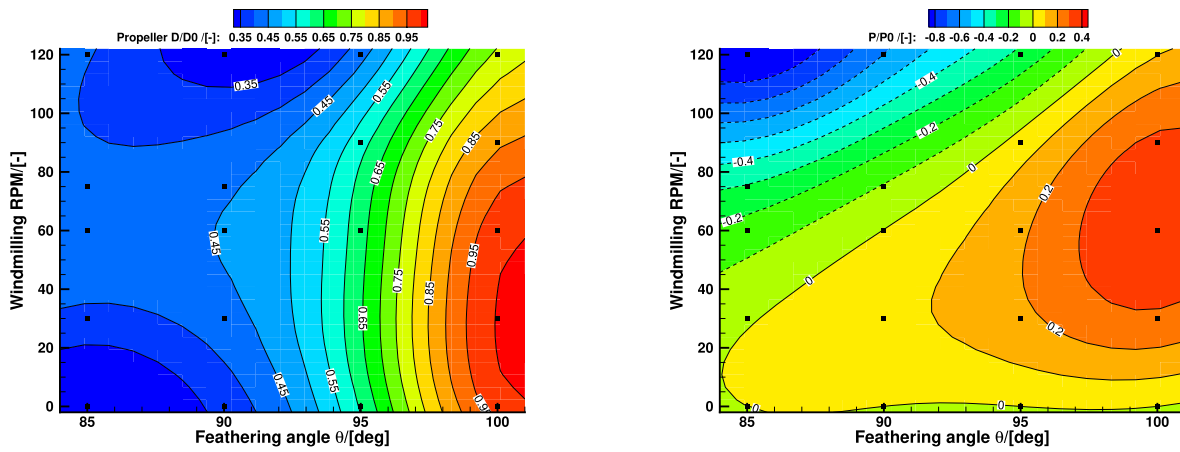
Fig. 17. Comparisons of pressure coefficients and tangential streamlines at the 25%, 50%, and 75% spanwise sections of the middle wing (Cases 2 and 3).

(a) Windmilling front propeller at $\theta = 95°$ and $RPM = 120$.

(b) Windmilling front propeller at $\theta = 100°$ and $RPM = 60$.
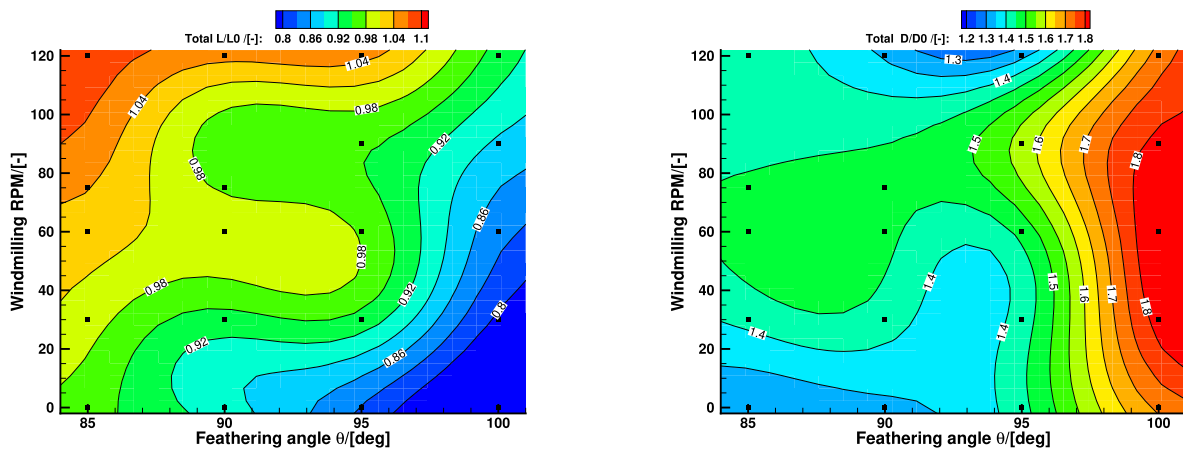
Fig. 18. Flow solutions of windmilling front propellers at different feathering angles and RPM (Case 4 of Table 1).

(a) Windmilling propeller drag variations (normalised with clean airframe drag D_0).

(b) Windmilling propeller power extractions (positive values denote energy extraction and negative values in dashed lines represent energy consumption). All values are normalised with clean airframe cruise power $P_0 = D_0 V_\infty$.

Fig. 19. Windmilling propeller drag and power extractions at different feathering angles and RPM (Case 4 of Table 1).

(a) Overall lift variations (normalised with clean airframe lift L_0).

(b) Overall drag variations (normalised with clean airframe drag D_0).

Fig. 20. Overall lift and drag variations at different feathering angles θ and windmilling RPM (Case 4 of Table 1). These are Kriging approximations, with the dots denoting sampling points.

Table 3
Vehicle performance comparisons with feathered and windmilling propellers in cruise (The signs of RPM denote different rotational directions).

Cases	Propeller conditions		
	Front	Middle	Aft
5.1	Feathered $\theta = 90°$	Feathered $\theta = 90°$	Thrusting $RPM = -365, \theta = 49.8°$
5.2	Windmill $RPM = 60, \theta = 95°$	Feathered $\theta = 90°$	Thrusting $RPM = -365, \theta = 49.8°$

6.2. Vehicle performance with windmilling and feathered propellers

This section further compares the feathering and windmilling performance on the vehicle level. As presented in Table 3, two extra cases were computed with all propellers installed on the airframe. Note that such multi-rotor configurations have plenty of options and redundancy for cruise operations [10], and the current study explored a particular choice. For both cases, the middle and front propellers were assumed redundant, and only the aft propellers were operating. This is to avoid excessive aerodynamic interference with downstream components due to the strong propeller wake.

For Case 5.1 of Table 3, both front and middle propellers were feathered with zero coning, zero azimuth shift, and $\theta = 90°$, which is close to the least drag angle and easy to implement. For this study, the vehicle trimming target was to have the net overall drag equal to zero. The trimming was performed by manually adjusting the aft propeller pitch angle as the simulations progress, upon an initial guess of the operating conditions. The overall vehicle drag in cruise was first estimated by summing up the isolated component drag from existing data. The required thrust was then estimated, and the aft propeller operating condition was interpolated from its performance map in isolation [10,12]. The blade pitch angle was slightly adjusted as the simulation progressed towards zero overall drag. The simulation adopted a one-degree-per-step temporal resolution for the aft propeller.

Case 5.2 was derived from Case 5.1 by allowing the front propeller to windmill. The front propeller feathering angle was set as 95 degrees, and the RPM was 1/6 of the aft propeller. This choice was interpolated from Figs. 19(a) and 19(b) considering the drag and power values. It did not bring the maximum energy extraction, but led to slightly lower front propeller drag. The simulation also adopted a one-degree-per-step temporal resolution for the aft propeller, which means 1/6-degree-per-step for the front propeller. Re-trimming of the aft propeller pitch angle was initially planned to counter the increased drag. However, for this particular case, no pitch change was introduced in practice, due to the increased aft propeller thrust benefiting from the upstream windmilling propeller wake.

The instantaneous flow solutions are shown in Figs. 21(a) and 21(b). These are pressure coefficient contours, and the transparent iso-surfaces are dimensionless Q-criteria illustrating the wake systems. The major difference is that the front propeller of Case 5.2 in Fig. 21(b) produced a helical and rotating wake for downstream components.

The time-averaged performance comparisons are presented in Table 4. The lift, drag, and power values are normalised with the clean airframe lift L_0, drag D_0, and required cruise power P_0, respectively, to highlight the relative changes. In terms of overall lift and drag, the windmilling brought minor changes. The overall drag was close to zero, and the negative values suggest minor net thrust forward. These small drag/thrust forces were the residual due to the manual trimming process.

The thrust propeller performance showed more differences due to the windmilling. As expected, the aft propeller of Case 5.2 produced about 0.18 D_0 higher thrust than the fully feathered Case 5.1. This was due to the slightly slowed inflow speed and swirl recovery brought by the windmilling. However, this thrust increase was also accompanied by a power consumption increase of 0.17 P_0. Nonetheless, the

windmilling front propeller extracted 0.19 P_0 from the free-stream. The overall power consumption of Case 5.2 was hence almost the same as the feathered Case 5.1.

These results indicate that windmilling could be a feasible alternative to feathering for redundant propellers in cruise, given adequately balancing of drag and power generation. However, it must be emphasised that the current promising windmilling results were obtained in highly idealised situations. We have assumed variable axial torque to allow for maximised power extraction, and we have neglected transmission and conversion losses. Taking these into consideration, the windmilling choice should be made with extra caution in practice.

7. Conclusions

Redundant and inoperative rotary wings are becoming common in the novel field of multi-rotor eVTOL designs. The current lack of understanding of their aerodynamic performance and downstream interference hinders their proper handling in cruise. This paper presented a systematic study of feathered and windmilling redundant propellers in cruise flight, through high-fidelity CFD simulations of a simplified multi-rotor, multi-wing model. Our study included variations of feathering angles, blade azimuth shift, conning angles, and a wide range of windmilling RPM and pitch settings, along with comparisons with the clean airframe without feathered blades. The analyses focused on the overall aerodynamic loading variations, and particularly on the aerodynamic interference to reveal the underlying mechanisms behind the loading changes. These results fill the knowledge gap concerning propeller redundancy, and provide valuable guidance for future multi-rotor eVTOL designs.

The following conclusions can be drawn from the current study:

1) For the feathered blades, the feathering angle showed dominant impacts on the overall aerodynamic loading, compared to azimuth shift and small conning angles. When the feathering angle was changed from 80 to 100 degrees, the overall lift dropped by 25% and the drag increased by 20%. The lift drop was associated with the front wing due to aerodynamic interference with the feathered blades, and drag was mainly due to the feathered blades. The six-bladed propeller, when feathered, produced a substantial drag ranging from 0.4 to 1.0 D_0 as feathering angle increased. This was due to the large propeller size and blade counts designed for hover operations. The middle wing's lift was almost constant subject to feathering angle growth, but the drag was interestingly decreased by about 75% due to aerodynamic interference. The aft wing and fuselage had little loading changes due to their clearance from upstream components. The feathered blade azimuth shift showed minor impacts due to the high blade counts leading to axial symmetry. The small conning angles ranging from -5 to 15 degrees resulted in negligible changes in the overall loading, but large conning angles imitating folding are expected to have significant effects.

2) Analyses of the high-fidelity flow solutions revealed that the aerodynamic interference between the feathered blades and the downstream lifting surfaces. The feathered blades altered the local flow directions for downstream wings, thereby changing the wing sectional effective AoA. The AoA changes altered the local lift and drag direction and magnitude. When these forces were projected back to body or global axes, they caused various overall lift and drag changes. The feathering angle hence had a dominant effect on the aerodynamic interference and the overall performance, as it directly changes the blade sectional AoA. The azimuth shift changed the position of these upstream blade sections, but did not alter the general phenomena. The small coning angles moved the blade sections slightly forward and backward, which had little impact on the interference. Large coning angles are expected to have significant impacts when the sectional displacements are substantial, such as folding.
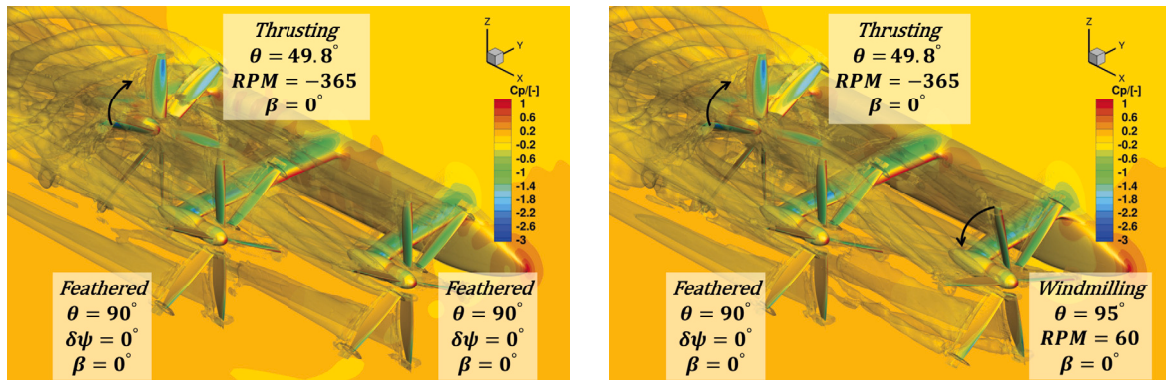
(a) Feathered front and middle propellers and thrusting aft propeller (Case 5.1 in Table 3).

(b) Windmilling front propeller, feathered middle propeller, and thrusting aft propeller (Case 5.2 in Table 3).

Fig. 21. Instantaneous flow solutions of the vehicle in cruise with all propeller installed as detailed in Table 4. These are pressure coefficient contours, and the transparent iso-surfaces are dimensionless Q-criteria illustrating the wake systems.

Table 4
Time-averaged vehicle cruise performance comparisons with feathered and windmilling propellers.

Cases	Total vehicle performance		Aft (thrusting) propeller performance		Windmilling power extraction P_e/P_0	Total power consumption P/P_0
	L/L0	D/D0	Thrust T/D0	Power consumption Pc/P0		
5.1	0.78	-0.10	1.98	2.70	-	2.70
5.2	0.79	-0.06	2.16	2.87	0.19	2.69

3) The loading variations of the downstream wings were correlated with the sectional AoA changes due to interference. As the feathering angle grew from 80 to 100 degrees, for the front wing, the blades induced strong downwash velocities that substantially reduced the local sectional AoA, causing about 50% reduced lift along with about 30% increased drag. The inner sections of the middle wing was subject to similar effects. The outer sections of the middle wing, however, was subject to the reversed effects. The feathered blades induced strong upwash on these sections due to the inverse blade camber and pitch in the upstream regions. The upwash increased the sectional AoA, leading to increased lift and reduced drag. In fact, due to the strong forward force projected by the lift, the net sectional pressure drag on the outer spans was negative (forward suction). The overall middle wing drag was of course still positive due to inner sections, the nacelle, and viscosity, but drag value was substantially reduced by 75%. The lift was almost constant as lift changes in the inner and out sections were balanced.

4) The propeller windmilling performance, while installed at the front wing's tip, was evaluated over a wide range of RPM and pitch combinations. The propeller was able to extract wind energy at high pitch angles. The peak ideal energy extraction was about 0.5 the required cruise power of the clean airframe, which happened at the 100-degree pitch angle and RPM 60. However, this was at the price of doubled overall drag compared to the clean airframe, and this drag increase was mostly associated with the propeller. The overall lift was reduced by about 15% compared to the clean airframe. A further performance comparison was made between the complete vehicles with feathered and windmilling front propellers, respectively. The overall performance were very similar despite the different propeller arrangements. Although the windmilling propellers caused more drag, the downstream thrusting propeller produced more thrust due to the slowed inflow, and the extracted wind energy compensated the overall energy consumption. However, it must be highlighted that these windmilling results were obtained in idealised conditions assuming zero conversion and transmission

loss. In practice, the windmilling option should be approached with careful consideration on the extra drag and power generation.

This paper has shown that redundant and inoperative propellers could have substantial impacts on the aircraft performance. These redundant propellers produce drag and can substantially change the downstream aerodynamic behaviour through interference effects. Folding or retracting the blades are effective solutions that can avoid these problems, but the mechanical difficulty should be accounted for. Feathering combined with partial folding could be a more practical option, but careful consideration on avoiding or exploiting the downstream aerodynamic interference is necessary. The current study focused on a single cruise flight condition. Future work will continue to explore more effective solutions for redundant propeller for novel eVTOL designs at various flight speeds and trimming conditions.

CRediT authorship contribution statement

Tao Zhang: Writing – review & editing, Writing – original draft, Visualization, Software, Investigation, Data curation. **G.N. Barakos:** Writing – review & editing, Writing – original draft, Supervision, Software, Resources, Project administration, Methodology, Investigation, Conceptualization. **Furqan:** Writing – review & editing, Methodology, Conceptualization.

Declaration of competing interest

The authors declare that they have no known competing financial interests or personal relationships that could have appeared to influence the work reported in this paper.

Data availability

Data will be made available on request.

References

[1] L. Kiesewetter, K.H. Shakib, P. Singh, M. Rahman, B. Khandelwal, S. Kumar, K. Shah, A holistic review of the current state of research on aircraft design concepts and consideration for advanced air mobility applications, Prog. Aerosp. Sci. 142 (2023) 100949.

[2] L. Veldhuis, Review of propeller-wing aerodynamic interference. ICAS 2004-6.3.1, in: 24th International Congress of the Aeronautical Sciences, Yokohama, Japan, 2004.

[3] T.C. Stokkermans, N. Van Arnhem, T. Sinnige, L.L. Veldhuis, Validation and comparison of RANS propeller modeling methods for tip-mounted applications, AIAA J. 57 (2) (2019) 566–580.

[4] T. Sinnige, T. Stokkermans, N. Van Arnhem, L.L. Veldhuis, Aerodynamic performance of a wingtip-mounted tractor propeller configuration in windmilling and energy-harvesting conditions, in: AIAA Aviation 2019 Forum, 2019, p. 3033.

[5] A. Bacchini, E. Cestino, B. Van Magill, D. Verstraete, Impact of lift propeller drag on the performance of eVTOL lift+ cruise aircraft, Aerosp. Sci. Technol. 109 (2021) 106429.

[6] O. Westcott, S. Krishna, R. Entwistle, M. Ferraro, Aerodynamic performance of aircraft wings with stationary vertical lift propellers, Aerosp. Sci. Technol. 141 (2023) 108552.

[7] H. McCOY, Full-feathering propellers, J. Aeronaut. Sci. 5 (7) (1938) 253–259.

[8] M. Beard, E. Fuller, Feathering propellers in airline transport operation, SAE Transact. (1939) 372–384.

[9] H. McCoy, Propeller design requirements, J. Aeronaut. Sci. 11 (3) (1944) 261–271.

[10] H. Frey, G.N. Barakos, M. Foster, et al., High-fidelity aerodynamic and acoustic design and analysis of a heavy-lift eVTOL, Aerosp. Sci. Technol. 137 (2023) 108307.

[11] J.P. Barnes, Regenerative electric flight synergy and integration of dual role machines, in: 53rd AIAA Aerospace Sciences Meeting, 2015, p. 1302.

[12] T. Zhang, G.N. Barakos, M. Foster, et al., Multi-fidelity aerodynamic design and analysis of propellers for a heavy-lift eVTOL, Aerosp. Sci. Technol. 135 (2023) 108185.

[13] G. Chirico, G.N. Barakos, N. Bown, Propeller installation effects on turboprop aircraft acoustics, J. Sound Vib. 424 (2018) 238–262.

[14] R. Steijl, G.N. Barakos, K. Badcock, A framework for CFD analysis of helicopter rotors in hover and forward flight, Int. J. Numer. Methods Fluids 51 (8) (2006) 819–847, https://doi.org/10.1002/fld.1086.

[15] M. Jarkowski, M. Woodgate, G. Barakos, J. Rokicki, Towards consistent hybrid overset mesh methods for rotorcraft CFD, Int. J. Numer. Methods Fluids 74 (8) (2014) 543–576, https://doi.org/10.1002/fld.3861.

[16] F. Menter, Two-equation eddy-viscosity turbulence models for engineering applications, AIAA J. 32 (8) (1993) 1598–1605, https://doi.org/10.2514/3.12149.

[17] R.J. Higgins, A. Zarev, G.N. Barakos, R.B. Green, Numerical investigation of a two-bladed propeller inflow at yaw, J. Aircr. 57 (2) (2020) 292–304.

[18] T. Zhang, G.N. Barakos, High-fidelity CFD validation and assessment of ducted propellers for aircraft propulsion, J. Am. Helicopter Soc. 66 (1) (2021) 1–28, https://doi.org/10.4050/JAHS.66.012008.

[19] T. Zhang, G.N. Barakos, High-fidelity numerical analysis and optimisation of ducted propeller aerodynamics and acoustics, Aerosp. Sci. Technol. 113 (2021) 106708, https://doi.org/10.1016/j.ast.2021.106708.

[20] A.J. Garcia, G.N. Barakos, Numerical simulations on the ERICA tiltrotor, Aerosp. Sci. Technol. 64 (2017) 171–191, https://doi.org/10.1016/j.ast.2017.01.023.

[21] G. Chirico, G.N. Barakos, N. Bown, Numerical aeroacoustic analysis of propeller designs, Aeronaut. J. 122 (1248) (2018) 283–315.

[22] R.J. Higgins, G.N. Barakos, S. Shahpar, I. Tristanto, A computational fluid dynamic acoustic investigation of a tiltwing eVTOL concept aircraft, Aerosp. Sci. Technol. 111 (2021) 106571.

[23] J. Sacks, S.B. Schiller, W.J. Welch, Designs for computer experiments, Technometrics 31 (1) (1989) 41–47, https://doi.org/10.1080/00401706.1989.10488474.

[24] M.A. Bouhlel, J.T. Hwang, N. Bartoli, R. Lafage, J. Morlier, J.R.R.A. Martins, A Python surrogate modeling framework with derivatives, Adv. Eng. Softw. (2019) 102662, https://doi.org/10.1016/j.advengsoft.2019.03.005.

[25] T. Zhang, G.N. Barakos, Development of simulation tools for high fidelity analysis of compound rotorcraft, in: AIAA Scitech 2020 Forum, 2020, p. 1258.

[26] T. Zhang, G.N. Barakos, Furqan, M. Foster, High-fidelity aerodynamic and acoustic evaluations of a heavy-lift eVTOL in hover, in: 49th European Rotorcraft Forum, Buckeburg, Germany, 2023.

[27] H. Sugawara, Y. Tanabe, Numerical investigation of rotor/wing aerodynamic interactions at high advance ratios, J. Aircr. 56 (6) (2019) 2285–2298, https://doi.org/10.2514/1.C035370.

[28] F. Frey, J. Thiemeier, C. Öhrle, M. Keßler, E. Krämer, Aerodynamic interactions on Airbus Helicopters' compound helicopter RACER in cruise flight, J. Am. Helicopter Soc. 65 (4) (2020) 1–14, https://doi.org/10.4050/JAHS.65.042001.

[29] J. Thiemeier, C. Öhrle, F. Frey, M. Keßler, E. Krämer, Aerodynamics and flight mechanics analysis of Airbus Helicopters' compound helicopter RACER in hover under crosswind conditions, CEAS Aeronaut. J. 11 (1) (2020) 49–66, https://doi.org/10.1007/s13272-019-00392-3.